THE PRECIPITATION OF ENERGETIC HEAVY IONS INTO THE UPPER ATMOSPHERE OF JUPITER

M. Horanyi*

Supercomputer Computations Research Institute

Florida State University

Tallahassee, Florida

T.E. Cravens

Space Physics Research Laboratory

Department of Atmospheric and Oceanic Science

The University of Michigan

Ann Arbor, Michigan 48109

J.H. Waite, Jr.

Marshall Space Flight Center

Huntsville, Alabama

February 1987

*On leave from Central Research Institute for Physics, Hungary

ABSTRACT

Evidence for auroral particle precipitation at Jupiter was provided by the ultraviolet spectrometers onboard the Voyagers 1 and 2 spacecraft and by the International Ultraviolet Explorer (IUE). Magnetospheric measurements made by instruments onboard the Voyager spacecraft indicate that energetic sulfur and oxygen ions are precipitating into the upper atmosphere of Jupiter. We have constructed a theoretical model describing the interaction of precipitating oxygen with the Jovian atmosphere. The auroral energy is deposited in the atmosphere by means of ionization, excitation, and dissociation and heating of the atmospheric gas. Energetic ion and electron precipitation are shown to have similar effects on the atmosphere and ionosphere of Jupiter.

I. INTRODUCTION

The ultraviolet spectrometers on the Voyagers 1 and 2 spacecraft (Broadfoot et al., 1981; Sandel et al., 1979) and the International Ultraviolet Explorer (IUE) satellite (Clarke et al., 1980; Yung et al., 1982) observed intense H_2 Lyman and Werner band emissions from the Jovian atmosphere at higher latitudes, and thus provided evidence for auroral particle precipitation at Jupiter. The Voyager ultraviolet spectrometer experiments (UVS) inferred about 60 kR of Lyman alpha emission and a total of about 80 kR of H_2 Lyman and Werner band emission if the latitudinal extent of the auroral zone was approximately 6000 km wide. This corresponds to an energy flux of 10 ergs/cm^2/s in the auroral zone, or a total global power of 1-2 x 10^{13} Watts if one identifies the precipitating particles as electrons (Waite et al., 1983; Atreya et al., 1981; Yung et al., 1982; Broadfoot et al, 1981; Gérard and Singh, 1982). Yung et al. (1982) interpreted IUE spectra of the Jovian aurora using a radiative transfer model for Lyman alpha and for the Lyman and Werner band emissions and they concluded that the precipitating electrons (if the particles are electrons) need to have energies between 1 and 30 keV. Waite et al. (1983) presented a comprehensive theoretical model of both the auroral and non-auroral atmosphere and ionosphere of Jupiter and used this model to explore the aeronomical effects of auroral precipitation of 1 and 10 keV electrons.

The Io plasma torus is thought to be the source of the energetic particles responsible for the observed aurora. Intense fluxes of charged particles have been detected in the inner magnetosphere of Jupiter by experiments on the Voyager spacecraft (Bridge et al., 1979; Krimigis et al., 1979; Vogt et al., 1979; Gehrels et al., 1981). Both the energetic and thermal ion populations in this region are largely composed of relatively heavy ions such as sulfur and oxygen. Most earlier magnetospheric studies of wave-particle interactions have suggested that electrons were more likely than ions to precipitate into the Jovian atmosphere (cf. Waite et al., 1983). Goertz (1980) suggested proton precipitation and Thorne (1981a, b) considered heavy

ion precipitation.

Gehrels and Stone (1983) reported on observations of 1 to 20 Mev/nucleon oxygen, sodium, and sulfur ions in the Jovian magnetosphere by the cosmic ray subsystem (CRS) onboard Voyagers 1 and 2. Gehrels and Stone (1983) (designated as GS, hereafter) calculated the inward diffusion rate of these heavy energetic ions and assumed that they are scattered into the loss cone, thus resulting in auroral power input into the Jovian atmosphere. We reproduce in Figure 1 the auroral power spectrum shown in Figure 12 of GS. This figure shows the calculated total integrated power as a function of energy for oxygen and sulfur. GS also extrapolated these spectra to energies below those actually observed by the CRS in order to obtain the 1-2 x 10^{13} W total auroral power required to explain the observed ultraviolet observations.

Some additional evidence in favor of ion (rather than electron) precipitation comes from X-ray observations of Jupiter made by the Einstein X-ray observatory (Metzger et al., 1983). Metzger et al. (1983) showed that if Bremstrahlung radiation from electron scattering was assumed then a total auroral power of 10^{15} - 10^{16} W would be required to explain the observed X-ray emission. They suggested that K-shell excitation of energetic precipitating S and O could explain the X-ray observations with a reasonable total power in line with that required by the ultraviolet observations.

This paper will investigate the nature of the energy deposition in the Jovian atmosphere by precipitating energetic oxygen ions and will explore the aeronomical effects associated with this deposition. The effects of energetic sulfur precipitation will not be considered explicitly; however, the general nature of the energy deposition should be independent of the exact atomic mass of a precipitating particle for comparable energies per nucleon.

The questions that this paper will seek to address are:

(1) How is the auroral power which is input at the top of the atmosphere distributed, or deposited, as a function of altitude?

(2) How is this deposited energy divided among various aeronomical processes such

as ionization, dissociation, heating, and optical emissions, etc.?

(3) How do these energy deposition efficiencies for various processes compare with the efficiencies calculated by Waite et al. (1983) for the precipitation of energetic electrons? In other words, how similar or different are the aeronomical effects of electron and heavy ion precipitation?

(4) What are the optical emissions associated with the precipitation of oxygen and sulfur ions? Can these emissions be used for an observational test of the existence of heavy ion precipitation at Jupiter?

Section 2 of the paper describes the physical processes included in both the energy deposition part of our theoretical model as well as the aeronomical part. In section 3, we present the results of the energy deposition calculations. We present the results of the aeronomical calculations in section 4; in particular, we show calculated atomic hydrogen density profiles and calculated electron and ion density profiles. Section 5 is a summary and discussion section. And in a companion paper (Waite et al., 1987) we present the results of some IUE observations of the Jovian aurora.

2. BASIC PROCESSES

The most important processes are charge-transfer, electron stripping, dissociative and non-dissociative ionization, excitation and elastic collisions. The competition between charge transfer and stripping determines the charge state of an oxygen ion at any given energy, but the bulk of the energy is lost via ionization processes. We have compiled the available data on the cross-sections for these processes, but in several cases we had to adopt various theoretical approximations to circumvent the lack of measured data. In our calculations we considered only four different charge states for the oxygen ions ($0 \leq q \leq 3$); the highest charge state is the triply ionized state.

In this section we give a detailed description of the processes followed by a description of the construction of the stopping power function using these processes. The method of equilibrated beams is employed. Finally, we discuss the energy distribution of the secondary electrons produced by the stripping and ionization processes.

2.1 The charge-transfer process

The charge transfer process can be represented as:

$$O^{q+} + X \rightarrow O^{(q-1)+} + X \qquad (2.1)$$

where X stands for the target which can be H or H_2.

The cross sections for process (2.1) are plotted in Figures 2 and 3 for the different charge states of the oxygen ions in H and H_2. The low energy cross sections are measured by Phaneuff et al. (1978), and the high energy cross sections by Phaneuff et al. (1982). For $q = 1$ oxygen ions in H_2 the low energy part was measured by Nutt et al. (1979). The continuous

lines in Figures 2 and 3 follow the data and the dashed lines are "graphical extrapolations".

Very little energy is lost by the oxygen during charge transfer collisions. Such collisions for q>1 are exothermic, although we have assumed a small energy loss of 1 eV in order to account for a certain fraction of collisions possibly resulting in oxygen excitation in excess of the exothermicity. The energy loss for charge-transfer collisions of O^+ was taken to be the endothermic energy plus 1 eV (accounting for possible excess excitation of the product O atoms), giving a total energy loss of 2.8 eV. The energy available to the products of charge transfer collisions (equation 2.1) for q=3 and for a H_2 target is 40.5 eV (including the additional loss of 1 eV mentioned above) and most of this energy should be available to excite the product O^{+2} ions so that O III emissions should be generated in a Jovian ion aurora. These emission features should appear below 1000Å in the spectrum. Similarly, 20.7 eV is available for the q=2 charge-transfer process resulting in O II emissions. The exothermic energy for these collisions ultimately comes from the beam kinetic energy via electron stripping collisions, which are discussed in Section 2.2.

2.2 The electron stripping process

The stripping (or electron removal) process can be represented as:

$$O^{(q-1)+} + X \rightarrow O^{q+} + X + e \qquad (2.2)$$

where X stands for H or H_2.

For this process we were unable to locate any measured cross section data for oxygen ions. The measured stripping cross-section of Goffe et al. (1979) for boron and carbon were very similar in both H and H_2. We assumed that the oxygen cross sections are also similar, and we used the Goffe et al. (1979) data for the q=2 and for q=3 states. As there was no data for the q=1 charge state, we constructed the cross-section for q=1 using the theoretical work of

Karasima and Watanabe (1983). The resulting cross-section functions are plotted in Figure 4.

The corresponding energy losses are the relevant ionization energies of oxygen (13.6 eV for q=1, 35.1 eV for q=2 and 54.9 eV for q=3) plus the average energy of the secondary electrons (T). We assumed that the energy distribution function of the secondary electrons emerging from stripping (and in the reference frame moving with the oxygen ions) is similar to the distribution for ionization at any given energy of the incident oxygen ion.

2.3 Ionization and excitation processes

The ionization of H can be represented by:

$$O^{q+} + H \rightarrow O^{q+} + H^{+} + e \qquad (2.3)$$

Shah and Gilbody (1981) measured the cross-section for this process for oxygen ions with $2 \leq q \leq 5$ in the energy range of $12 \leq E \leq 195$ keV/amu. Part of their data is plotted with thick lines in Figure 5. These measurements indicate that the ionization cross sections for oxygen ions with $q > 1$ are roughly independent of the charge state in the energy range below where the cross sections have their maxima; but at higher energies, where the cross sections have decreased below their maximum values, the cross sections scale with q as:

$$\sigma_{i} \sim q^{1.46} \qquad (2.4)$$

To supplement these experimental results we used the calculations of Olson et al. (1978). They calculated the cross section for electron removal from H (that is, the sum of the cross sections of charge transfer and ionization, σ_T). They did this for ions with $1 \leq q$

≤ 50 in the energy range of $50 \leq E \leq 5000$ keV/amu, and their results fall on a single curve given by the expression:

$$\sigma_T = 4.6qA(1 - \exp(-A))\ 10^{-16} \qquad (2.5)$$

where $A = 32q/E$, E has units of keV/amu and s_T is in units of cm^2.

We assumed that the experimental trends evident for $q > 1$ were also valid for $q = 1$ as well, and we used the measured data together with equation (2.5) to construct cross section functions for $q = 1$ and to extend the energy range for $q = 2$ and $q = 3$ cross section functions.

We could not locate data in the literature for $q = 0$. Stripping and ionization are basically the same process if the projectile and target atoms are both neutral, and one calls it stripping or ionization depending on whether or not the target or the projectile is ionized. Hence, ionization and stripping cross sections for $q = 0$ should be very similar; we have assumed that these cross sections are the same. Information on the stripping of H in collisions with various heavier neutral targets was also used in trying to construct a realistic cross section (McNeal and Birely, 1973). The resulting cross section functions are plotted in Figure 5. The energy loss for these processes is the sum of the ionization energy (13.6 eV) and the average energy of the secondary electrons (T).

The ionization process for H_2 is more complicated than for H, as there are several possible final channels. For example:

$$O^{q+} + H_2 \rightarrow O^{q+} + H_2^+ + e \qquad (2.6a)$$

$$O^{q+} + H_2 \rightarrow O^{q+} + H^+ + H + e \qquad (2.6b)$$

$$O^{q+} + H_2 \rightarrow O^{q+} + 2H^+ + 2e \qquad (2.6c)$$

The dominant channel is non-dissociative ionization. These ionization processes can be divided into two groups: the non-dissociative part (equation 2.6a) and the dissociative part, which is the sum of all channels leading to the dissociation of H_2. The thick continuous dashed lines in Figure 6 represent the measured data for non-dissociative and dissociative ionization processes, respectively. The thin lines are extrapolations based on the same (perhaps questionable) arguments that we adopted for H. The q = 0 ionization cross section for H_2 was constructed in almost the same way as the H ionization cross section discussed above.

The energy loss in the non-dissociative channel is the sum of the ionization energy (15.4 eV) and the average energy of the secondary electrons ($\overline{T}$). The energy loss in the dissociative channel can be approximated as the sum of the dissociation energy of the H_2 molecule (4.5 eV), the ionization of an H atom (13.6 eV) and the average energy of the secondary electrons ($\overline{T}$).

To estimate the cross section function for excitation of H and H_2 we assumed them to be proportional to the ionization cross-section for H and to the non-dissociative ionization cross section for H_2, respectively. We assumed a proportionality factor of 0.6, independent of the incident energy and the charge state of the oxygen ion. The ratio of the total excitation cross section to the ionization cross section for electron impact on H_2 is approximately 0.6 at higher energies. The majority of this excitation is to the $B^1\Sigma_g^+$ and $C^1\Pi$ states resulting in Lyman and Werner band emission.

2.4 The equilibrium fractions

If the collision mean free path is less than the atmospheric scale height, then the population distribution of the different charge states in the incident ion beam will reach an equilibrium distribution at any given energy. Let us denote that fraction of oxygen ions with charge state q as ϕ_q, with the normalization condition:

$$\sum_{q} \phi_q = 1 \tag{2.7}$$

Naturally, the ϕ_q depend on the energy of the beam. The time evolution of the ϕ_q are governed by the equation:

$$\frac{d\phi_q}{dt} = \sum_{q'} (\phi_{q'} P_{q'q} - \phi_q P_{qq'}) \tag{2.8}$$

where $P_{qq'}$ is the transition probability in unit time from the charge state q to q'. Assuming that charge distribution is in equilibrium ($d\phi_q/dt = 0$) and that only processes with a change of one electron are important ($P_{qq'} = P\,\delta_{q', q\pm1}$), we find the conditions of the detailed balance:

$$\phi_q P_{q,q+1} = \phi_{q+1} P_{q+1, q} \tag{2.9}$$

Equation (2.9) can be solved for each ϕ_q at any given energy by replacing the transition probabilities with the cross-sections for stripping ($P_{q,q+1}$) and charge transfer ($P_{q,q-1}$). The resulting equilibrium charge distributions are plotted in Figures 7 and 8 for H and H_2, respectively. The results show that below approximately 10 keV/amu the majority of the oxygen particles in both H and H_2 will be neutral. With increasing energy, higher and higher charge states become dominant. The highest charge state we considered was q = 3 which actually includes all higher charge states as well (equation 2.3). Consequently, our calculated stopping power (discussed in subsection 2.6) becomes increasingly inaccurate for E>300 keV/amu.

2.5 Elastic collisions

At high energies ions lose very little energy through elastic collisions with the nuclei of the medium, but this is no longer true at lower energies where the average net charge of the ion approaches zero. While the electronic part (inelastic collisions) of the stopping power is dropping to zero with decreasing ion energy, the average loss from the elastic collisions is increasing rapidly.

We adopted the universal nuclear stopping-power function from Lindhard et al. (cf. Northcliffe and Schilling, 1970), which was based on the Thomas-Fermi interaction model. The nuclear and electronic (to be described later) parts of the stopping power are plotted in Figure 9.

2.6 The stopping power

We are primarily interested for the present study in the range of energy ($1.0 \leq E \leq 300$ keV/amu), which is well below the range of validity of the Bethe formula. The only information we were able to locate in the literature was the range and stopping power tables of Northcliffe and Schilling (1970) which does not contain any information about the individual processes and whose lowest energy point is at 12 keV/amu. Based on the individual cross-section data which we have compiled (and in some cases extrapolated) one can determine the stopping power function:

$$S(E) = \frac{-dE}{ndx} = S_e + S_n \qquad (2.10)$$

where n is the number density of the target medium. The stopping power S is the sum of the electronic stopping power (due to inelastic collisions) S_e, and the nuclear stopping power (due to elastic collisions) S_n.

The electronic part of the stopping power is:

$$S_e = \sum_q \sum_i \phi_q \sigma_i^q \quad \Delta E_{qi} \tag{2.11}$$

where σ_i^q and ΔE_{qi} are the cross section and energy loss, respectively, for oxygen ions of charge state q and for the i-th process. Replacing ϕ_q with their equilibrium values we can directly calculate S_e.

In Figure 9 we have plotted separately the two parts of the stopping power for H_2 and, for comparison, the relevant stopping power from the Northcliffe and Schilling (1970) tables as well. The stopping power for H is very close to half of that for H_2. Below approximately 200 keV/amu, our calculated stopping power is in reasonable agreement with the Northcliffe data, but at higher energies the difference is more significant. There are several possible reasons for the discrepancy. In the low energy regime we have more confidence in our results and despite the uncertainties of the cross section data we do not believe that the Northcliffe tables are any more reliable. At higher energies ($E \geq 200$ keV/amu) , however, the buildup of charge states with $q > 3$ will introduce errors into our calculated stopping power, causing an underestimation of stripping and ionization cross sections which increases with charge state q.

2.7 The energy distribution of secondary electrons

To circumvent the lack of measured data for the energy distribution of secondary electrons produced in the ionization or stripping processes, we have assumed that the shape of the energy distribution function of the secondary electrons is independent of the charge state of the incident particle, and that it is the same for ionization and stripping in the frame of reference of the electron emitting species (i.e., H or H_2 for ionization and O for stripping). With these assumptions we can use the partial differential cross section of

secondary electrons for proton collisions with H_2 measured by Rudd (1979) to represent the shape of the secondary electron distribution for oxygen collisions on H and H_2, These relative cross sections versus secondary electron energy were then integrated and normalized using the total ionization cross sections (integrated over all secondary electron energies), which were taken from Figures 5 and 6.

We used the empirical fit of Rudd (1979) to the measured distribution function:

$$\sigma(Y,T) = 5\pi a_0^2 \, \alpha^3 \sum_i \frac{N_i I_H^2 \, (Y/I_i)}{I_i^3 \, (4 + (Y/I_1)^2)} \, \exp\left[\frac{-aT}{I_i Y}\right] \qquad (2.12)$$

where T is the energy of the secondary electron in eV, $Y = E_p/1836$, E_p is the incident proton energy in eV, a_0 is the radius of the first Bohr orbit (0.529×10^{-8}), $I_H = 13.6$ eV, a = 1.28 and N_i is the number of electrons in the target with binding energy I_i. We assume that E_p is the oxygen energy per amu. The electron production cross section for stripping, σ (Y,T), is not given by equation (2.12), but is determined by a transformation of equation (2.12) to the oxygen frame of reference. This was done numerically. Figure 10 shows relative differential cross section for the stripping process as a function of electron energy for several primary energies. At low primary energies the relative cross section is almost the same as the ionization cross section (equation 2.12), but at higher energies the transformation to the oxygen reference frame shifts the cross sections to larger values of T.

The agreement of equation (2.12) with the experimental ionization data is good below approximately 50 keV incident proton energy for all secondary electron energies. For proton energies above 50 keV, the low energy part of the secondary electron distribution is well represented by equation (2.12), but at higher electron energies the fit deviates from the data. For all incident oxygen energies we used equation (2.12) to calculate the average energy of the secondary electrons:

$$\bar{T} = \frac{\int_0^\infty T\sigma(Y,T)dT}{\int_0^\infty \sigma(Y,T)dT} \qquad (2.13)$$

where I is the average ionization energy (≈ 15 eV) for H_2. One finds that $\bar{T} = IY^{1/2}/2$ for ionization, but is greater than this for stripping. The final value of $\bar{T}$ is determined by weighting the T for both ionization and stripping with the respective total cross sections.

2.8 Basic Processes for Secondary Electrons

The secondary electrons, produced by the interaction of the energetic ion beam with the H_2 and H in the upper atmosphere of Jupiter, will themselves interact with the neutral atmosphere. These electrons can ionize, dissociate, electronically excite, and vibrationally excite H_2 molecules, as well as heat the ambient thermal electrons in the ionosphere. Most secondary electrons for atmospheric densities greater than ≈ 2 x 10^9 cm^{-3} (i.e., altitudes less than ≈ 750 km) have mean free paths less than an atmospheric scale height and deposit their energy locally. But electron transport is important at higher altitudes.

The two-stream method is used in our model to calculate secondary electron (and photoelectron) fluxes and the associated energy deposition rates for various processes. This method was described in Banks and Nagy (1970) and Nagy and Banks (1970). The pitch angle distribution of electrons is approximated by two streams, one going up parallel to the magnetic field, and the other going down. The energy bin width was 0.5 eV for electron energies less than 10 eV, 1 eV for energies greater than 10 eV and less than 100 eV, and various larger bin widths were used for more energetic electrons. The electron impact cross section data for H_2 and H used in the model was discussed by Waite et al. (1983).

2.9 Aeronomical Processes

Energy deposition drives a variety of aeronomical processes in the upper atmosphere of Jupiter. For example, dissociation of H_2 by energetic particles and their secondary electrons produces H atoms which diffuse down to the homopause region where they participate in hydrocarbon chemistry and eventually recombine. And ionization of H_2 and H by energetic particles, or by solar radiation, leads to the formation of an ionosphere. For this paper, we used the aeronomical model described by Waite et al. (1983) and Waite (1981).

The neutral temperature structure for the Jovian thermosphere was taken from interpretations of Voyager UVS stellar and solar occultation data by Atreya et al. (1981) and Festou et al. (1981). The neutral part of the model solves the continuity and momentum equations for H_2, He, H, CH_4, CH_3, C_2H_2, C_2H_4, and C_2H_6, and also for the major ion in the ionosphere, H^+. Photochemical solutions were obtained for $C_2H_5^+$, CH_5^+, CH_4^+, CH_3^+, CH_2^+, CH^+, He^+, HeH^+, H_2^+, and H_3^+. The ionospheric and neutral models were coupled with the energy deposition model so that consistent solutions are obtained. Ionization by solar extreme ultraviolet radiation was also included, as described in Waite et al. (1983); however, energy deposition by energetic particles (ions or electrons) is much more important than solar radiation in the Jovian auroral regions.

The momentum equation for neutrals includes both molecular and eddy diffusion. We used an eddy diffusion coefficient of:

$$K = 10^6 \ (10^{13}/M)^{1/2} \ \ cm^2 s^{-1} \qquad (2.13)$$

where M is the total atmospheric number density. This choice of K gives reasonable agreement between calculated densities of CH_4, C_2H_2, and C_2H_6 near the homopause and hydrocarbon mixing ratios inferred from Voyager UVS stellar occultation results (Atreya et

al., 1981)

Both the neutral temperature structure and the eddy diffusion coefficient were derived for low latitudes, and not for the higher latitude auroral regions. Auroral heating and the associated thermospheric circulation will certainly alter the neutral atmosphere at higher latitudes. However, to a large extent the energy deposition (and even the associated aeronomy) of energetic precipitating particles does not greatly depend on the details of the atmosphere structure if one uses atmospheric density level, rather than altitude, as the independent variable. In this paper, we will often include in the relevant figures both an altitude scale and a scale for total neutral number density (which is almost equal to the molecular hydrogen density except at the highest altitudes where H is relatively abundant).

3. ENERGY DEPOSITION

The total power delivered to the Jovian atmosphere by energetic oxygen and sulfur ions as a function of energy was determined by Gehrels and Stone (1983)(see Figure 1). We assumed that the power for both oxygen and sulfur was all in the oxygen ions since our cross section data is for oxygen. We also assumed that the energy spectrum could be fit with a power law which was also applied to energies much less than those which were actually measured (Gehrels and Stone, 1983). When the total energy flux is transformed to a particle flux (per unit energy) one obtains a $E^{-3.1}$ power law where E is the energy. Fluxes per unit area were obtained by assuming that the precipitating ions were incident on auroral zones 6000 km wide, centered at 65° latitude in both hemispheres. 48 discrete beams with incident energy, E_k (k=1,48), were used to represent the incident ion energy spectrum from 0.1 keV/amu up to 1 Mev/amu (see Table 1). The energy bin width for beam k is $\Delta E_k = (E_{k+1} - E_{k-1})/2$. The net downward incident particle flux for beam k is:

$$F_k = 2 \times 10^4 \, E_k^{-3.1} \, \Delta E_k \quad (cm^{-2} \, s^{-1}) \tag{3.1}$$

where E_k and ΔE_k are in units of MeV/amu.

The calculations in this paper used equation (3.1) with a range of lower energy cutoffs, E_{min}. However, the paper emphasizes the calculation for E_{min} = 40 keV/amu (or k≥15); that is, we assumed zero input flux for E less than E_{min} and used equation (3.1) for higher energies. The total power per unit area for this choice of E_{min} is 15 ergs/cm^2/s which corresponds to a total global power of approximately 2 x 10^{13} W. E_{min} = 40 keV/amu was chosen so that the calculated intensity of the H_2 Lyman and Werner band emissions was approximately the 80 kR or so observed by the UVS experiment on V1 and V2 (Broadfoot et al., 1979, 1981). The total power per unit area required for precipitating 10 keV electrons to produce the same H_2 Lyman and Werner band emission is 10

ergs/cm^2/s (Waite et al., 1983).

The downward pitch angle distribution was assumed to be isotropic and we put all the flux in at an "average" pitch angle with $\langle\cos\alpha\rangle = 0.5$. The energy of an ion (or an ion beam k) as a function of altitude can be found from its initial energy at the top of the atmosphere by using the stopping power:

$$E(z) = E_0 \; -2 \int_{z_{top}}^{z} S\,[\,E(z')\,]\; n(z')\; dz' \qquad (3.2)$$

where z_{top} = 3350 km, n(z) is the neutral density at z, the stopping power S is from equations (2.9) and (2.10) The energy at the top of the atmosphere, E_0, is equal to E_k. Actually, we included the densities and stopping power for both H_2 and H, although only H_2 is important except at higher altitudes. The factor of 2 in equation (3.2) accounts for ratio of pathlength increment to altitude increment for the average pitch angle used. Note that the energy refers to the energy of an equilibrated beam composed of several charge states.

The total energy deposition rate at a given altitude (in units of eV/cm^3/s) for beam k, $Q_k(z)$, can be found from the energy for beam k at altitude z, E(z), and from the stopping power:

$$Q_k\,(z) \;=\; 2\,F_k\; n(z)\; S[E(z)] \qquad (3.3)$$

where the factor of 2 is from the averge pitch angle. Again, both H_2 and H were included. The energy deposition rate at z for a complete spectrum is found by adding up the appropriate $Q_k(z)$ for the desired range of k. The energy deposition rate for a particular process, rather than the total deposition rate, is found by using only the relevant part of the stopping power S in equation (3.3).

3.1 Total Energy Deposition Rates Versus Cutoff Energy

Total energy deposition rate profiles are shown in Figure 9 as functions of altitude (an atmospheric density scale is also provided) for a range of cutoff energies, E_{min}. The neutral atmosphere model used for these calculations is called "unconverged" which means that the H densities are small and only take into account solar processes (Waite et al., 1983). This atmosphere is mostly H_2 up to an altitude of ≈ 900 km. The H densities for the "converged" atmosphere are much larger and include in a self-consistent manner the H produced by the energetic ion precipitation. The maximum energy deposition rates in Figure 9 increase with decreasing values of E_{min} since more energy is input at the top of the atmosphere. And the altitude of this maximum deposition also increases with decreasing values of E_{min} since less energetic oxygen does not penetrate as deeply into the atmosphere. The lowest energy in the Voyager energetic ion data is somewhat above 300 keV/amu (Gehrels and Stone, 1983). The deposition rate profile for this cutoff has a peak at an altitude of 400 km (total number density of ≈ 10^{13} cm^{-3}) and has a total integrated power which is only about 10% of that required to explain the observed UV emissions from H_2. The homopause and the top of the hydrocarbon layer are both located approximately at 350 km in the equatorial region, but are possibly located at higher altitudes for higher latitudes, so that ions more energetic than 300 keV/amu will penetrate into this layer.

3.2 Energy Deposition Rate For 40 keV/amu Cutoff Energy

A total energy input of 15-20 ergs/cm^2/s is required to generate the observed UV airglow intensity, and in order to obtain this input from the power spectrum, a cutoff energy, E_{min} = 40 keV/amu is required. This requires an extrapolation in the observed

energetic ion spectrum by about a factor of 10 in both particle energy and total power (Gehrels and Stone, 1983). Figure 10 shows the energy deposition rate profile for this cutoff energy. The peak deposition rate is 1.1 x 10^6 eV/cm^3/s at an altitude of 430 km (n_{tot}=3.8 x 10^{12} cm^{-3}). The total integrated energy deposition rate is 15 ergs/cm^2/s, or 9.25 x 10^{13} eV/cm^2/s, giving a global power of 2 x 10^{13} W.

Some breakdown of how the beam energy is deposited in the atmosphere is also indicated in Figure 12. The ionization and the charge-transfer/stripping processes account for most of the deposited energy. About 33% of this energy is put into secondary electrons; and the rest goes into ionization of molecular hydrogen and excitation of the energetic oxygen. Excitation of H_2 is not a major loss process for the oxygen beam but still accounts for about half of the required UV emissions. We assume that the vast majority of H_2 excitation leads to Lyman and Werner band emission either directly or via cascade from higher-lying allowed levels. Nuclear/elastic collisions are not a very important energy loss process, and this energy ends up as part of the total neutral heating rate as will be discussed later.

The fractional contributions of each charge state in the equilibrated beam to the energy deposition are shown in Figure 13 as functions of altitude. Energy deposition by O^+ (q=1) and O^{++}(q=2) dominates near the top of the atmosphere, as might be expected from the equilibrium fractions for energies in the 40 -100 keV/amu range (Figurs 7 and 8). As the precipitating ions penetrate deeper into the atmosphere and lose energy, the equilibrium fractions of q=0 and q=1 become larger and these charge states dominate the energy deposition. However, very deep in the atmosphere the contributions of the q=2 and 3 states begin to pick up again because the lower energy part of the input spectrum has completely degraded and only more energetic ions remain.

3.3 Energy Deposition by Secondary Electrons

The secondary electron distribution (see section 2) is strongly weighted towards lower energies. Figure 12 shows the production rate of electrons as a function of electron energy, T, for an altitude of 450 km and for the input spectrum with E_{min} = 40 keV/amu. The shape of the production rate curve at other altitudes is very similar to this one, although the total altitude-integrated electron production rate is just equal, at each altitude, to the total electron production rate. The total electron production from the primary beam is due both to direct ionization and to stripping collisions as shown in Figure 12. Total H_2^+ and H^+ production rates (including ionization by both the primary beam and by secondary electrons, and including the contribution due to the charge-transfer process) are shown in Figures 15 and 16.

The two-stream method was used to calculate the upward and downward electron fluxes (ϕ^+ and ϕ^-, respectively) as a function of electron energy and altitude. Figure 15 displays ϕ^+ and ϕ^- versus altitude for a typical electron energy of T = 9.25 eV. Notice that $\phi^+ = \phi^-$ except for altitudes greater than $\approx$ 750 km, well above the altitude of peak energy deposition. This is an indication that the electrons degrade and deposit their energy in the near vicinity of where they were produced and that electron transport is not important. Some electrons do escape at higher altitudes where the mean free path becomes long compared to an atmospheric scale height. Figure 18 shows the differential electron flux as a function of energy for an altitude near the peak of the energy deposition (z = 450 km). The shape of this distribution reflects both the shape of the electron production energy distribution (i.e., Figure 14) and the energy dependence of the electron impact crosssections.

Electrons with energies greater than the ionization potentials of atomic or molecular hydrogen can generate further secondary ionization. Figures 15 and 16 also show the contribution of secondary ionization processes to the total ionization rates. Secondary electrons also electronically excite H_2 and H (producing Lyman and Werner band emission and Lyman alpha emission), and vibrationally excite and dissociate H_2 .

The altitude dependence of these various processes is very similar to that of seconda ionization (Figure 15) and will not be shown. The altitude integrated rates (that is, c production rates) for all these processes will be discussed in the next section.

3.4 Column Production Rates and Energy Deposition

We have integrated the production rates over altitude for all important pr for oxygen precipitation with E_{min} = 40 keV/amu. The contributions of the primar beam and the secondary electrons are distinguished. The fraction of the total input deposited in the atmosphere via a particular process -- as determined by the column efficiency -- is also calculated. Table 2a lists these results for the unconverged atm (low H densities) and Table 2b for the converged atmosphere (large H densities). T energy input is 15 ergs/cm^2/s for the 40 keV/amu cutoff energy and the total calcula Lyman and Werner band intensity is 66 kR which is in rough agreement with the V UVS results. The contributions of the primaries and the secondaries are about the Lyman and Werner band excitation. The H_2 band excitation for the converged atn is about 20% smaller than for the unconverged atmosphere because more energy i deposited in H for the former than for the latter. On the other hand, the converge atmosphere has much more Lyman alpha emission than does the unconverged at

Ionization is the most important process, accounting for about 45% of energy input. "Ionization energy" here refers to the production rate times the ior potential and does not include the energies of the secondary, or teritary, electror accounted for seperately. H_2^+ production is larger than H^+ production for both atmospheres. Most of the energy put into H_2^+ production eventually ends up a heat due to ion-neutral chemistry and ion recombination (Waite et al., 1983). T beam is much more important than secondary electrons for the ionization proc

Secondary electrons are more important than the primary ion beam

processes such as direct dissociation of H_2 (resulting in H production), direct vibrational excitation of H_2, and electron heating. For these processes, electrons with energies below ≈ 12 eV make the greatest contribution. However, vibrational excitation can also result from the cascading associated with Lyman and Werner band emission. Similarly, some H production and some neutral heating is associated with H_2^+ production because this ion typically reacts with H_2 in the Jovian atmosphere to produce H_3^+ and H plus some excess energy. Most of the H_3^+ then recombines dissociatively providing H and heat. Similarly, almost all of the energy put into vibrational excitation, electron heating, and dissociation also ends up eventually as neutral heat due to various quenching, recombination, and cooling processes. The net total neutral heating efficiency is close to 47% for the unconverged atmosphere, and is a couple percent less than this for the converged atmosphere.

A significant part of the energy deposited by the energetic oxygen via the electron stripping process reappears during charge-transfer collisions as excitation energy of the product energetic oxygen ions or atoms (10%). We estimate that ≈ 5% of the total input energy ends up as excitation of oxygen in its various charge states. (The other 5% is attributed to sulfur.) This excitation should appear as optical emissions mainly from OI, OII, and OIII with a total intensity over all spectral features of roughly 40 kR. Most of these spectral features are below 1000 A in the spectrum and should include spectral features observed by the Voyager UVS from the Io plasma torus. But since we have assumed that energetic sulfur acts like oxygen in its energy deposition and have only performed the calculations for the latter, there should really only be about 20 kR of excited oxygen emission and the remaining 20 kR or so should come from excited sulfur species. Furthermore, some incident oxygen and sulfur are also probably excited directly via collisions with the ambient H_2; however, we have no information concerning this type of process and have neglected it, assuming it is less important than excitation via the stripping/charge transfer process. This is discussed further later in the paper.

The miscellaneous category in the Tables represents: (1) energy put into processes not explicitly accounted for, such as rotational excitation, (2) errors in assigning specific energy losses for the various processes, (3) and errors in the calculation. For example, there is a several percent error due to not accurately keeping track of the beam energy in the last (and lowest) altitude bin for a given beam. Kozyra et al. (1981) showed that almost all of this energy ends up as neutral heat, so that one can consider that a large part of the energy in the miscellaneous category is neutral heat.

One of the goals of this paper is to compare the atmospheric effects of electron and ion precipitation. Table 3 is a comparison of the column energy efficiencies for ion precipitation (Table 2a) and 10 keV electron precipitation (from Table 5a of Waite et al., 1983). The peak of the energy deposition profile for the 10 keV electron aurora is at 460 km, almost the same altitude as the peak of the deposition rate for the oxygen beam with E_{min} = 40 keV/amu. The efficiencies for H_2^+ production and for assorted "low energy" processes (i.e., direct vibrational excitation, electron heating, direct neutral heating, direct H production) are very similar for the two types of auroral precipitation. However, oxygen precipitation is more efficient than electron precipitation for either H^+ production or oxygen (and sulfur) excitation. But electrons are more efficient than the oxygen beam for Lyman alpha excitation and Lyman and Werner band excitation, which is why an energy input of 15 ergs/cm^2/s, or more, energy input is required for the oxygen beam and only 10 ergs/cm^2/s for electron precipitation. However, the error in the calculation of the emission rates for the oxygen beam is roughly equal to this difference. Overall, the energy deposition patterns for the two types of auroral precipitation are rather similar, especially taking into account the uncertainties in both sets of calculations.

4. AERONOMICAL EFFECTS OF ENERGETIC ION PRECIPITATION

It was established in the last section that the pattern of energy deposition for electron and heavy ion precipitation is about the same, within a factor of two or so. The aeronomy associated with auroral precipitation depends on where in the atmosphere the energy is deposited as well as on the total amount of energy deposited. The altitude of the peak energy deposition for the precipitation of magnetospheric oxygen with energies in excess of 40 keV/amu is about the same as for the precipitation of 10 keV electrons (z = 460 km which is equivalent to a total atmospheric density of 3×10^{12} cm^{-3}), and, consequently, the aeronomical effects of the two types of auroral precipitation are similar. Waite et al. (1983) demonstrated that both the neutral atmosphere and the ionosphere are greatly altered by electron precipitation, and in this section we will show that this is also true for oxygen precipitation.

4.1 Neutral Atmosphere

The total column heating efficiency for the neutral thermospheric gas should take into account: (1) the direct heating due to the dissociation of molecular hydrogen by electron or ion impact, (2) electron heating because this heat ultimately goes to the thermospheric neutrals because the electrons cool via electron-neutral collisions, (3) vibrational excitation because virtually all of this energy ends up as thermal energy due to the collisional de-activation of the vibrationally excited H_2 , (4) chemical heating associated with chemical reactions initiated by H_2^+. Recombination of H can be neglected as a heat source above the homopause. Waite et al. (1983) found that the total neutral heating efficicency for electron precipitation was very close to 50% for both 1 keV and 10 keV electrons. We calculated this total heating efficiency for ion precipitation by adding up the relevant entries in Table 2, and we obtained a value of 47%, which is the same as the electron precipitation value within the error.

The neutral thermospheric temperature profile can be determined by solving the energy

equation including heat conduction, heating processes, and cooling processes. The neutral temperature calculated in this manner by Waite et al. (1983) was 1000-2000 K higher for the auroral case than for the case with solar EUV heating only. We will not repeat this calculation for the ion aurora because the resulting temperature profile would be the same for equal auroral energy inputs, because the heating efficiency is the same for electron and ion precipitation and because the altitude of the maximum heating is almost the same (for 10 kev electrons). The temperatures one would calculate for an ion aurora would be somewhat larger than for an electron aurora, because the Lyman and Werner band excitation efficiency is about a factor of two less for ions than for electrons, so that a larger incident power is required to obtain the observed intensities for the former.

Neutral composition is also affected by auroral energy deposition. In particular, the abundance of atomic hydrogen should be very large in auroral regions because dissociation of molecular hydrogen, both directly by particle impact and indirectly due to photochemical reactions initiated by H_2^+, is greatly enhanced in auroral situations. Altitude profiles of H_2, H, and He densities are displayed in Figure 19. The curve labeled "unconverged" designates the H density profile calculated without any auroral precipitation; the peak density is about 10^{10} cm^{-3}. The H profile labeled "converged" was calculated including the auroral production of H. The composition and the precipitation/energy deposition parts of the model were iterated until convergence was achieved. The peak H density for the auroral case is 4×10^{11} cm^{-3}; this is very close to the peak density obtained by Waite et al. for 10 keV electron precipitation. Both sets of auroral calculations ignore the possible dilution of H in the auroral regions due to horizontal transport of H out of these regions via the thermospheric winds generated by the auroral thermospheric heating.

Vibrationally excited molecular hydrogen is another component of the neutral atmosphere strongly affected by auroral precipitation (Cravens, 1987). But again, the total energy input and location in the atmosphere is more important than the species of the precipitating particles. The column energy efficiency for vibrational excitation is about

20% for either incident electrons or ions. Cravens (1987) calculated the distribution of vibrationally excited for several scenarios including the 10 keV auroral precipitation case considered by Waite et al. (1983). It is reasonable to assume that if these vibrational calculations were re-run using ion aurora inputs, then the results would be similar to the 10 keV electron aurora results.

4.2 The Ionosphere

Ionization rates are greatly enhanced in the auroral regions and it was shown in the last section that this is true for ion as well as electrons. The production efficiency for H_2^+ is almost the same for the two types of aurora, although the peak production rate for ion aurora must be somewhat larger due to the somewhat larger incident power needed to produce the observed intensities of Lyman and Werner band emissions. However, the efficiency for H^+ production is 3 times greater for ion precipitation than for electrons. In both cases, H^+ is the major ion even though the production rate of H_2^+ is much higher than that of H^+. The reason is that for standard models in which radiative recombination is the most important loss process for H^+, the chemical lifetime of this ion is much longer than the lifetime of other ions such as H_2^+ and H_3^+(c.f., Atreya and Donahue, 1976). H_2^+ is rapidly converted to H_3^+ via the following reaction:

$$H_2^+ + H_2 \rightarrow H_3^+ + H \tag{4.1}$$

Then the H_3^+ ions are rapidly removed via dissociative recombination:

$$\begin{aligned} H_3^+ + e &\rightarrow H_2 + H \\ &\rightarrow H + H + H \end{aligned} \tag{4.2}$$

The density of H_3^+ depends both on the production rate of H_2^+ and on the rate coefficient for reaction (4.2); we have used the rather small value of 10^{-8} cm^3 s^{-1} in agreement with recent theoretical and experimental results (Michels and Hobbs, 1984; Smith and Adams, 1984; MacDonald et al., 1984).

The calculated density profiles for H_3^+ and H^+, as well as electrons, are shown in Figure 20. The densities of H_2^+ and other molecular ions are extremely small and are not shown. H_3^+ becomes the major ion only at altitudes well below the ionospheric peak. H^+ is the major ion at higher altitudes and the maximum electron density is 3×10^7 cm^{-3}. The peak electron density for the10 keV electron aurora was only 1.5×10^7 cm^{-3} (Waite et al., 1983), which is reasonable considering that: (1) the peak H^+ production rate for the ion aurora is about 4 times larger than it was for the electron aurora and, (2) the electron density varies as the square root of the production rate for a major ion in photochemical equilibrium. In any case, the observed electron densities at higher latitudes on Jupiter (Eshleman et al., 1979) are about a factor of 100 smaller than the calculated values. Clearly, some additional loss mechanism is required for the H^+ ions and several mechanisms have been suggested (cf., Atreya et al, 1979; Waite and Cravens, 1986) including the reaction with vibrationally excited H_2 with $v \geq 4$:

$$H^+ + H_2(v \geq 4) \rightarrow H_2^+ + H \qquad (4.3)$$

Cravens (1987) demonstrated that this can be a potent loss process in the auroral region. This result should be as applicable to an ion aurora as to an electron aurora.

Connerney and Waite (1984) suggested another loss process that might be operating as a sink of H^+ ions on Saturn. Water vapor entering the top of the atmosphere from the rings could act as a chemical sink, converting ionospheric protons to H_2O^+ ions which have a short lifetime. A similar process might operate in the Jovian ionosphere if heavy ion precipitation is occuring. The energetic O ions/atoms eventually neutralize and thermalize.

They will then diffuse downward. If the thermal oxygen density is sufficiently large then H^+ ions could be removed via a charge exchange reaction:

$$H^+ + O \rightarrow O^+ + H \qquad (4.4)$$

The reaction rate coefficient for this is about 10^{-9} cm^3 s^{-1} (Banks and Kockarts, 1973) and an O density of roughly 10^5 cm^{-3} near the ionospheric peak would be sufficient for this reaction to compete with radiative recombination as a removal mechanism for H^+. The O^+ ions are rapidly removed by reaction with H_2 molecules:

$$O^+ + H_2 \rightarrow OH^+ + H \qquad (4.5)$$

OH^+ will recombine dissociatively reforming the original O atom. We are currently looking into this mechanism in more detail.

5. K-SHELL X-RAY EMISSION FROM OXYGEN AND SULFUR

X-ray observations of the Jovian aurora were made by the Einstein X-ray Observatory (Metzger et al., 1983). Metzger et al. (1983) estimated that a total auroral power of 10^{15} - 10^{16} W would be required to explain the observed emissions if they were due to Bremsstrahlung associated with energetic electron precipitation. However, they estimated that a total power of only 10^{13} - 10^{14} W would be required to explain the observations with K shell excitation of the precipitating oxygen and sulfur ions. The X-ray photons for K shell excitation of oxygen and sulfur are 540 eV and 2300 eV, respectively. The total power required to explain the observations in this way was 5×10^9 W at the lower energy and 4-8 x 10^8 W at the higher energy (Metzger et al., 1984).

We have calculated K shell emission rates using our model. Our model is only applicable to oxygen but we can assume that the pattern of energy deposition for precipitating oxygen and sulfur is very similar and apply the model to both species. We used the K shell excitation cross sections of Garcia et al. (1973) and for the x-ray emission efficiencies of sulfur and oxygen, we used 10% and 0.8% respectively. The K-shell excitation cross sections are very small for ion energies less than 100 keV/amu, and they are proportional to q^2 where q is the charge on the ion. As a result, only the more energetic part of the incident auroral beam contributes to K-shell excitation.

The calculated energy efficiencies (relative to the total auroral power for both oxygen and sulfur, and assuming equal energy inputs for both species) for X-ray emission are 4 x 10^{-6} and 8 x 10^{-7} for oxygen and sulfur, respectively. Using these efficiencies, one finds that the total power required to explain the X-ray observations is 0.7 - 1.5 x 10^{15} W. However, there is a serious source of error in these figures. Our model is quite inaccurate for energies in excess of 200 keV/amu or so because we terminate our equilibrium charge state at q=3, although at higher energies the actual values of q can be significantly larger. This is not a serious problem for the overall energy deposition since 90% of the incident

energy flux is for ions with energies less than approximately 200 keV/amu; however, it is a serious problem for K-shell excitation. We estimate that the "average" value of q at higher energies is 4-6, and the corrected K-shell excitation cross section then becomes about 4 times larger than we used. The revised total power required to explain the X-rays is now about 2×10^{14} W. This value refers to all incident ions in excess of 40 keV/amu. However, if one were to truncate the energy spectrum at about 200 keV/amu, then the X-ray excitation rate would be affected very little and the total auroral power required would be $1\text{-}3 \times 10^{13}$ W. This auroral power is a factor of ten greater than that deduced by Gehrels and Stone (1983) from the magnetospheric measurements for these incident ion energies; however, there are uncertainties in the deduced auroral energy input, in the X-ray observations, and in our calculations of the K shell excitation efficiencies.

6. ULTRAVIOLET EMISSIONS FROM PRECIPITATING OXYGEN AND SULFUR

The oxygen ions/atoms in the incoming auroral beam can be directly excited via collisions with the atmospheric gas.

$$O^q + H_2 \rightarrow O^{q+*} + H_2 \qquad (6.1)$$

O^{q+} can also be excited during a charge transfer collision:

$$O^{(q+1)+} + H_2 \rightarrow O^{q+*} + H_2^+ \qquad (6.2)$$

Reaction (6.2) is highly exothermic for $q > 1$, and the product oxygen ion is likely to be highly excited and/or the H_2^+ ion dissociated. See the companion paper by Waite et al. (1987) for additional discussion of these processes. These excitation mechanisms also apply to sulfur.

Two emission features in particular which should be present in the auroral spectra measured at Jupiter are the OI 1304 A line and the SII 1256 A line. Waite et al. (1987) reported on IUE observations of the Jovian aurora in the 1240 - 1500 A spectral region. The measured intensities at 1256 and 1304 A were at the noise level, and upper limits of 2kR and 150 R, respectively, were set for these two features. First, consider the direct excitation mechanism. Waite et al. estimated that the excitation cross section of O colliding with H_2 was 4% of the electron removal/stripping cross section for O. Our calculations show that the column rate of electron stripping for O is 5×10^{10} cm^{-2} s^{-1} if the entire incident beam is composed of oxygen and 2.5×10^{10} cm^{-2} s^{-1} if the beam is half oxygen and half sulfur. The estimated OI 1304 A intensity is 1 kR if one multiplies this latter number by the 4% emission efficiency. 1 kR is a factor of 10 larger than the upper limit set by the IUE measurements.

Now consider the charge-transfer excitation mechanism. The total column energy deposition efficiency (for all charge states) that is available for exciting the product

ions/atoms from the charge transfer process is close to 10% (see section 4). The corresponding column energy dissipation for this process is $\approx 10^{12}$ eV/cm^2/s for a total auroral power input of $\approx 10^{13}$ W. Following the discussion given by Waite et al. (1987) we can make the following estimates of O and S spectral intensities. Suppose that half of the available energy goes into dissociating the product H_2^+ ions and half into exciting the product O and S ions/atoms. The total column emission rate for all S and O features is then $\approx$ 20 kR for a typical UV photon energy of 20 eV or so. There are approximately 10 strong emission features in the UV spectra of these two species, so that one can expect that roughly 2 kR is emitted per spectral feature (on the average) for SI, SII, SIII, SIV, and OI, OII, and OIII (Waite et al., 1987). None of these features in the IUE spectral range (and in particular, SII 1256 A) have intensities much above the noise level in the IUE spectra.

7. DISCUSSION

One goal of this paper, and of the companion paper by Waite et al., was to ascertain whether or not auroral ion precipitation is occurring on Jupiter. Another goal was to determine how heavy ion precipitation affects the upper atmosphere and ionosphere of Jupiter. Our basic conclusion concerning this second point is that the energy deposition and the associated aeronomy are very much alike for both electron and ion precipitation. For example, about 30-40% of the incident auroral power goes into ionizing H_2 for both types of auroras. However, there are also some differences. Energetic ions are three times more effective than electrons in producing H^+ ions (if one extrapolates the Gehrels and Stone spectra to lower energies). And energetic electrons are approximately twice as effective as ions (14% versus 7%) for the excitation of the H_2 Lyman and Werner bands. One consequence of this latter difference is that a column energy input of 20 ergs/cm^2/s is needed for ion precipitation to generate 80 kR of these features, whereas only 10 ergs/cm^2/s is needed for electrons. The input for our model was only 15 ergs/cm^2/s, and thus only 66 kR was produced. These are minor differences, though; basically, the two types of precipitation have similar effects on the atmosphere. The H densities and the electron densities calculated for the two types of particle precipitation are the same within a factor of 2.

We will now briefly discuss how likely ion precipitation is at Jupiter. A more complete discussion of this issue is provided in the companion paper. Measurements of energetic sulfur and oxygen in the Jovian magnetosphere which were made by instruments on the Voyager spacecraft (Gehrels and Stone, 1983) suggested that these ions were being lost via pitch-angle scattering and subsequent auroral precipitation of these ions. The X-ray observations made by the Einstein Observatory also support the existence of ion precipitation (Metzger et al., 1983). However, other magnetospheric evidence suggests

that electron precipitation is also taking place (cf., Waite et al., 1987). The lack of observed O and S emissions in the UV also throws some doubt on the degree of S and O precipitation.

The following scenario might be able to reconcile the conflicting evidence concerning ion versus electron precipitation. Magnetospheric O and S does precipitate, but only for energies in excess of 100 - 300 keV/amu; that is $E_{min} \approx$ 200 keV/amu. This does not contradict the Voyager measurements of Gehrels and Stone (1983) since the ions they observed exceeded even this energy. The total input power of energetic ions is now about 2×10^{12} W and the beam will penetrate deep into the atmosphere (see Figure 11). The excitation rates for the H_2 Lyman and Werner bands and for the S and O UV features are now all a factor of 10 smaller. The UV intensities are even smaller if the beam penetrates the hydrocarbon layer where UV photons can be absorbed. The predicted S and O line intensities will now be in line with the upper limits set by the IUE observations. Of course, the Lyman and Werner band intensities will also be much reduced, and will now be less than 10 kR; some other mechanism (such as electron precipitation) is now required to produced the observed intensity of $\approx$ 80 kR. The K-shell emission rates for O and S remain almost unaffected by the increase in E_{min}; they are still somewhat too small, but one is no worse off with the new scenario than one was with the "full" ion aurora. A combination of uncertainties might be able to explain the discrepancy between the model and observed X-ray intensities.

In summary, we are suggesting that: (1) energetic S and O ions with energies in excess of 100-300 keV/amu, and with a total power of $\approx 10^{12}$ W, are precipitating into the upper atmosphere of Jupiter and that these ions can partially or entirely explain the observed X-ray emissions, and (2) energetic electrons with incident energies in excess of 10 keV and a total power of $\approx 10^{13}$ W are also precipitating and explain the bulk of the observed Lyman and Werner band emissions. Atmospheric and ionospheric processes are not very sensitive to the identity of the precipitating particles (i.e., electrons, heavy ions, or protons)

but depend only on the total amount of energy deposited in the atmosphere and on the atmospheric level at which this energy is deposited.

Acknowledgement: This research was supported by NASA grants NAGW-312 and NAGW-15. One of us (M.H.) acknowledges support from the Department of Energy under the agreement number No. DE-FC05-85ER25000.

References

Atreya, S.K., and T.M. Donahue, Model ionospheres of Jupiter, in Jupiter, edited by T. Gehrels, pp. 304-318, University of Arizona Press, Tucson, 1976.

Atreya, S.K., T.M. Donahue, and J.H. Waite, Jr., An interpretation of the Voyager measurements of Jovian electron density profiles, Nature, 280, 795-796, 1979.

Atreya, S.K., T.M. Donahue, and M.C. Festou, Jupiter: Structure and composition of the upper atmosphere, Astrophys. J., 247, L43, 1981.

Banks, P.M., and A.F. Nagy, Concerning the influence of elastic scattering upon photoelectron transport and escape, J. Geophys. Res., 75, 1902, 1970.

Banks, P.M., and G. Kockarts, Aeronomy, Academic Press, New York, 1973.

Bridge, H.S., J.W. Bekher, A.J. Lazarus, J.D. Sullivan, R.L. McNutt, F. Bagenal, J.D. Scudder, E.C. Sittler, G.L. Siscoe, V.N. Vasyliunas, C.K. Goertz, and C.M. Yeates, Magnetic field studies at Jupiter by Voyager 1: Preliminary results, Science, 204, 982, 1979.

Broadfoot, A.L., M.J.S. Belton, P.Z. Takacs, B.R. Sandel, D.E. Shemansky, J.B. Holbert, J.M. Ajello, S.K. Atreya, T.M. Donahue, H.W. Moos, J.L. Bertaux, J.E. Blamont, D.F. Strobel, J.C. McConnell, A. Dalgarno, R. Goody, and M.B. McElroy, Extreme ultraviolet observations from Voyager 1 encounter with Jupiter, Science, 204, 979, 1979.

Broadfoot, A.L., B.R. Sandel, D.E. Shemansky, J.C. McConnell, G.R. Smith, J.B. Holberg, S.K. Atreya, T.M. Donahue, D.F. Strobel, and J.L. Bertaux, Overview of the Voyager ultraviolet spectrometer results through Jupiter encounter, J. Geophys. Res., 86, 8259, 1981.

Clarke, J.T., H.W. Moos, S.K. Atreya, and A.L. Lane, Observations from earth orbit and variability of the polar aurora on Jupiter, Astrophys. J., 241, 179-182, 1980.

Connerney, J.E.P., and J.H. Waite, New model of Saturn's ionosphere with an influx of water from the rings, Nature, 312, 136-138, 1984.

Cravens, T.E., Vibrationally excited molecular hydrogen in the upper atmosphere of Jupiter, J. Geophys. Res., in press, 1987.

Eshleman, V.R., G.L. Tyler, G.E. Wood, G.F. Lindal, J.D. Anderson, G.S. Levy, and T.A. Croft, Radio science with Voyager 1 at Jupiter: Preliminary profiles of the atmosphere and ionosphere, Science, 204, 976-978, 1979.

Festou, M.F., S.K. Atreya, T.M. Donahue, B.R. Sandel, D.E. Shemansky, and A.L. Broadfoot, Composition and thermal profiles of the Jovian upper atmosphere determined by the Voyager stellar occultation experiment, J. Geophys. Res., 86, 5715, 1981.

Garcia, J.D., R.J. Fortner, and T.M. Kavanagh, Inner-shell vacancy production in ion-atom collisions, Reviews of Modern Physics, 45, 111-177, 1973.

Gehrels, N., E.C. Stone, and J.H. Trainor, Energetic oxygen and sulfur ions in the Jovian magnetosphere, J. Geophys. Res., 86, 8906, 1981.

Gehrels, N., and E.C. Stone, Energetic oxygen and sulfur ions in the Jovian magnetosphere and their contribution to the auroral excitation, J. Geophys. Res., 88, 5537-5550, 1983.

Gerard, J.-C., and V. Singh, A model of energy deposition of energetic electrons and EUV emission in the Jovian and Saturnian atmospheres, J. Geophys. Res., 87, 4525, 1982.

Goertz, C.K., Proton aurora on Jupiter's nightside, Geophys. Res. Lett., 7, 365-368, 1980.

Goffe, T.V., M.B. Shah, and H.B. Gilbody, One-electron capture and loss by fast multiply charged boron and carbon ions in H and H_2, J. Phys. B.: Atom. Molec. Phys., 12, 3763-3773, 1979.

Karashima, S., and T. Watanabe, Charge equilibrium of energetic heavy ions in gaseous media (Ideal atomic hydrogen gas), Japanese J. Appl. Phys., 22, 895-902, 1983.

Kozyra, J.U., T.E. Cravens, and A.F. Nagy, Energetic O^+ precipitation, J. Geophys. Res., 87, 2481-2486, 1982.

Krimigis, S.M., T.P. Armstrong, W.S. Axford, C.P. Bostrom, C.Y. Fan, G. Gloeckler, L.J. Lanzerotti, E.P. Kearth, R.D. Zwickl, J.F. Carbary, and D.C. Hamilton,

Low-energy charged particle environment at Jupiter: A first look, UScience, 204, 998, 1979.

McNeal, R.J., and J.H. Birely, Laboratory studies of collisions of energetic H^+ and hydrogen with atmospheric constituents, Rev. Geophys. Space Phys., 11, 633-642, 1973.

Macdonald, J.A., M.A. Biondi, and R. Johnsen, Recombination of electrons with H_3^+ and H_5^+ ions, Planet. Space Sci., 32, 651-654, 1984.

Metzger, A.E., D.A. Gilman, J.L. Luthey, K.C. Hurley, H.W. Schnopper, F.D. Seward, and J.D. Sullivan, The Detection of X-rays from Jupiter, J. Geophys. Res., 88, 7731-7741, 1983.

Michels, H.H., and R.H. Hobbs, Low-temperature dissociative recombination of e + H_3^+, Astrophys. J., 286, L27-L-29, 1984.

Nagy, A.F., and P.M. Banks, Photoelectron fluxes in the ionosphere, J. Geophys. Res., 75, 6260, 1970.

Northcliffe, L.C., and R.F. Schilling, Range and Stopping-power tables for heavy ions, Nuclear Data Tables, A7, 233-464, 1970.

Nutt, W.L., R.W. McCullough, and H.B. Gilbody, Electron capture by 0.1-13 keV C^+, N^+, and O^+ ions in H and H_2, J. Phys. B.: Atom. Molec. Phys., 12, L157-L162, 1979.

Olson, R.E., K.H. Berkner, W.G. Graham, R.V. Pyle, A.S. Schlacthter, and J.W. Stearns, , Phys. Rev. Lett., 41, 163-166, 1978.

Phaneuf, R.A., F.W. Meyer, and R.H. McKnight, Single-electron capture by multiply charged ions of carbon, nitrogen, and oxygen in atomic and molecular hydrogen, Phys. Rev. A., 17, 534-545, 1978.

Phaneuf, R.A., I. Alvarez, F.W. Meyer, and D.H. Crandall, Electron capture in low-energy collisions of C^{q+} and O^{q+} with H and H_2, Phys. Rev. A., 26, 1892-1905, 1982.

Rudd, M.E., Energy and angular distributions of secondary electrons from 5-100 keV proton collisions with hydrogen and nitrogen molecules, Phys. Rev. A., 20, 787-796, 1979.

Sandel, B.R., D.E. Shemansky, A.L. Broadfoot, J.L. Bertaux, J.E. Blamont, M.J.S. Belton, J.M. Ajello, J.B. Holberg, S.K. Atreya, T.M. Donahue, H.W. Moos, D.F. Strobel, J.C. McConnell, A. Dalgarno, R. Goody, M.B. McElroy, and P.Z. Takacs, Extreme ultraviolet observation from Voyager 2 encounter with Jupiter, Science, 206, 962-966, 1979.

Shah, M.B., and H.B. Gilbody, Experimental study of the ionization of atomic hydrogen by fast multiply charged ions of carbon, nitrogen, and oxygen, J. Phys. B: Atom. Molec. Phys., 14 2831-2841, 1981.

Smith, D., and N.G. Adams, Dissociative recombination coefficients for H_3^+, HCO^+, N_2H^+, and CH_5^+ at low temperature: Interstellar implications, Astrophys. J., 284, L13-16, 1984.

Thorne, R.M., Jovian auroral secondary electrons and their influence on the Io plasma torus, Geophys. Res. Lett., 8, 509, 1981a.

Thorne, R.M., Microscopic plasma processes in the Jovian magnetosphere, in Physics of the Jovian Magnetosphere, chapter 12, edited by A.J. Dessler, Cambridge University Press, New York, 1981b.

Vogt, R.E., W.r. Cook, A.C. Cummings, T.L. Garrard, N. Gehrels, E.C. Stone, J.H. Trainor, A.W. Schardt, T. Conlon, N. Cal, and F.B. McDonald, Voyager 1: Energetic ions and electrons in the Jovian magnetosphere, Science, 204, 1003, 1979.

Waite, J.H., Jr., The ionosphere of Saturn, Ph.D. thesis, University of Michigan, Ann Arbor, 1981.

Waite, J.H., Jr., T.E. Cravens, J.U. Kozyra, A.F. Nagy, S.K. Atreya, and R.H. Chen, Electron precipitation and related aeronomy of the Jovian thermosphere and ionosphere, J. Geophys. Res., 88, 6143-6163, 1983.

Waite, J.H., Jr., and T.E. Cravens, A current review of the Jupiter, Saturn, and Uranus ionospheres, paper presented at COSPAR, Toulouse, France, 1986.

Waite, J.H., Jr., J.T. Clarke, and T.E. Cravens, The Jovian aurora: Electron or ion precipitation?, J. Geophys. Res., submitted, 1987.

Yung, Y.L., G.R. Gladstone, K.M. Chang, J.M. Ajello, and S.K. Srivastava, H2 fluorescence spectrum from 1200 to 1700 Å by electron impact: Laboratory study and application to Jovian aurora, Astrophys. J., 254, L65, 1982.

FIGURE CAPTIONS

Figure 1 Total integrated power for precipitating oxygen and sulfur ions versus oxygen/sulfur energy. From Gehrels and Stone (1983).

Figure 2 Charge transfer cross sections versus oxygen energy for oxygen ions of different charge states in atomic hydrogen.

Figure 3 Charge transfer cross sections versus oxygen energy for oxygen ions of different charge states in molecular hydrogen.

Figure 4 Electron stripping cross sections versus energy for oxygen ions of different charge states in atomic and molecular hydrogen.

Figure 5 Cross sections for the ionization of atomic hydrogen versus energy for different oxygen charge states.

Figure 6 Cross sections for the ionization of molecular hydrogen (dissociative and non-dissociative) versus energy for different oxygen charge states.

Figure 7 Equilibrium fractions of an oxygen beam in various charge states versus energy for atomic hydrogen.

Figure 8 Equilibrium fractions of an oxygen beam in various charge states versus energy for molecular hydrogen.

Figure 9 Stopping power (or loss function) as a function of oxygen energy for an oxygen beam in molecular hydrogen. The nuclear (elastic) contribution is shown separately. The stopping power from Northcliffe and Schilling (1970) is also shown.

Figure 10 Relative differential ionization cross sections versus electron energy for collisions of oxygen ions at various energies with molecular hydrogen, but only for the electron stripping process.

Figure 11 Energy deposition rate as a function of altitude on Jupiter for incident oxygen beams whose energy spectra have the lower energy cut-offs indicated.

Figure 12 Energy deposition rate as a function of altitude for an incident oxygen beam whose energy spectrum is a power law (see text) for energies in excess of 40 keV/amu but with zero flux below this cutoff energy. Contributions of different types of collisions (or processes) to the total energy deposition are shown. A total atmospheric number density scale(mostly H_2) is provided on the righthand side of the figure.

Figure 13 Fractions of the energy deposition contributed by collisions of oxygen in different charge states (as labeled) in molecular hydrogen. The total energy deposition rate relative to these curves is shown in Figure 12. The sum of these fractions for all charge states does not add to 1 because some of the energy is being deposited into H and not into H_2, especially at higher altitudes.

Figure 14 The production rate of secondary electrons versus electron energy, at an altitude of 450 km for an incident oxygen spectrum with a 40 keV/amu cutoff.

Figure 15 Production rate of molecular hydrogen ions versus altitude on Jupiter for an incident oxygen beam with a 40 keV/amu cutoff. Production from solar extreme ultraviolet (EUV) radiation is also included. Contributions to the total H_2^+ production rate are shown for different processes (primary oxygen ions, secondary electrons, and solar EUV radiation).

Figure 16 Similar to Figure 15 but for the production of H^+ ions. H^+ ions can either be produced via direct ionization of H by primary oxygen ions, secondary electrons, or solar EUV radiation, or by dissociation ionization of H_2 via the various types of collisions.

Figure 17 Differential secondary electron flux directed both up and down as a function of altitude for an electron energy of 25 eV. The incident oxygen beam had a lower energy cutoff of 40 keV/amu.

Figure 18 Differential secondary electron flux, at a fixed altitude, as a function of electron energy. The electron distribution at this altitude is almost isotropic.

Figure 19 Number densities of molecular hydrogen, atomic hydrogen, and helium versus altitude. The curve labeled unconverged represents H density calculated without auroral energy input and only with solar radiation input. The curve labeled converged represents the H density calculated with the ion aurora turned on, and after convergence of the program.

Figure 20 Calculated ionospheric profiles (H_3^+ and H^+ ions, and total electron density) versus altitude for the ion aurora with "converged" H densities.

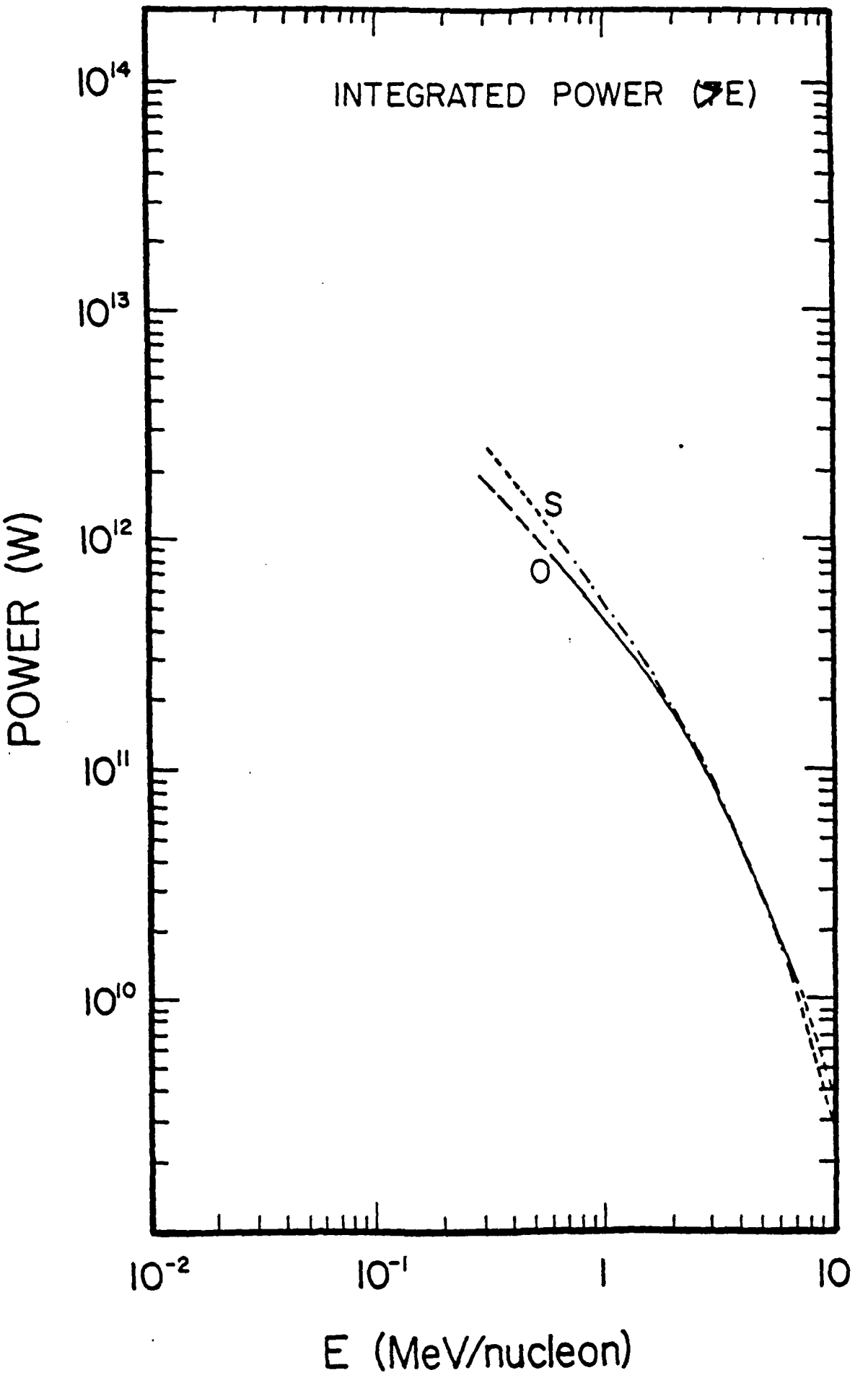
INTEGRATED POWER (∫E)
POWER (W)
10^{14}
10^{13}
10^{12}
10^{11}
10^{10}
S
O
10^{-2}
10^{-1}
1
10
E (MeV/nucleon)

FIGURE 1

HORANYI

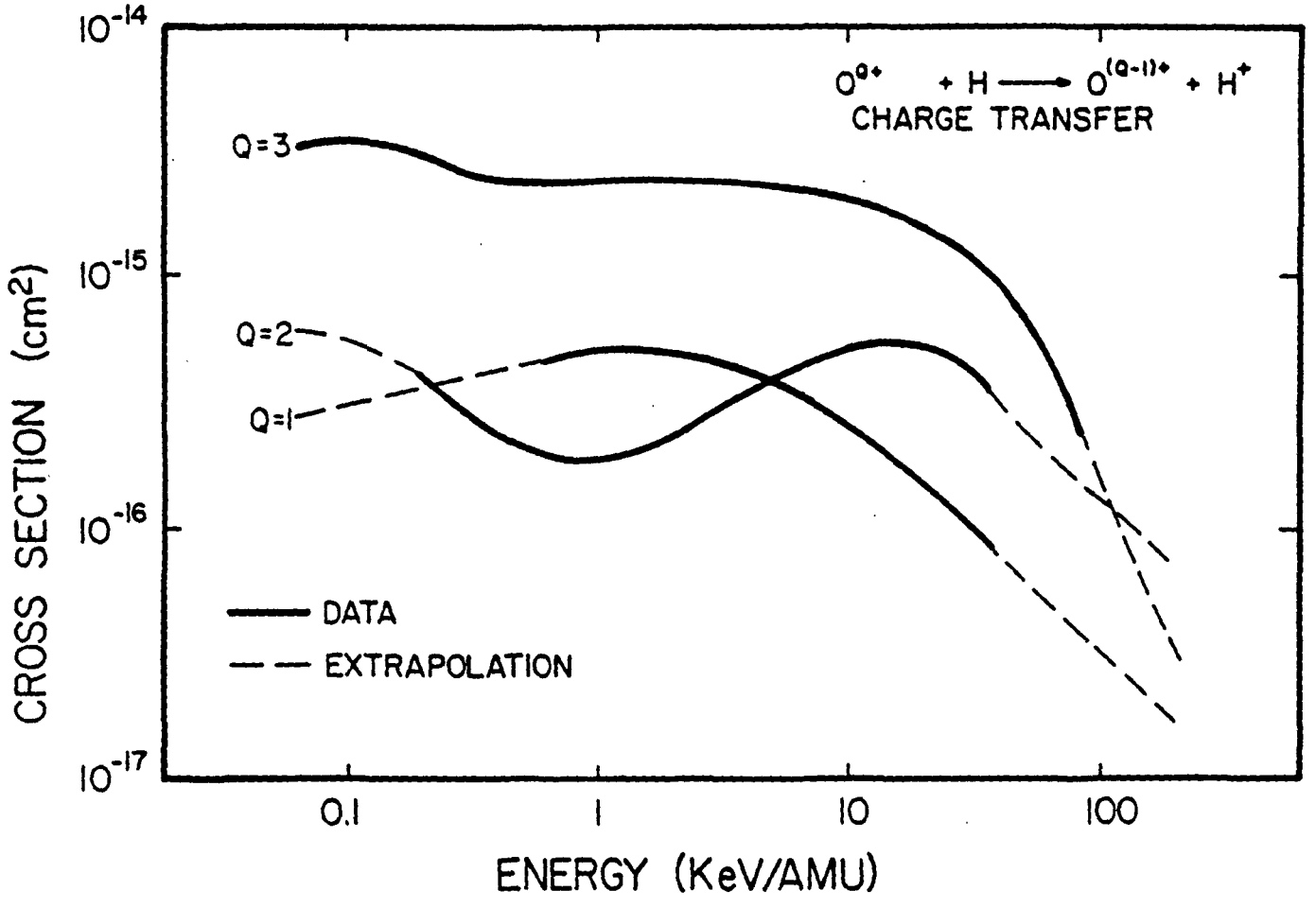

FIGURE 2

ORANYI

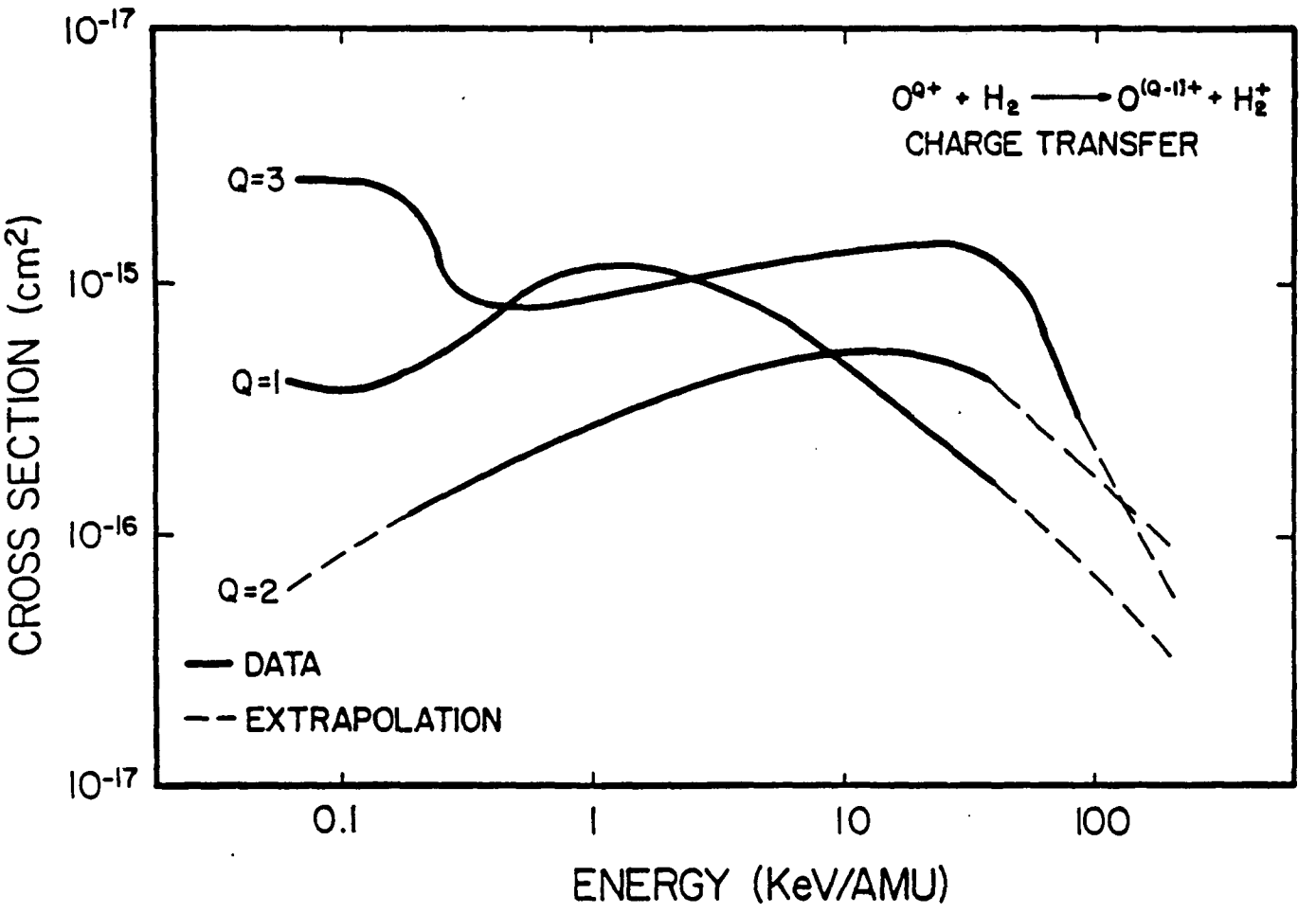

FIGURE 3

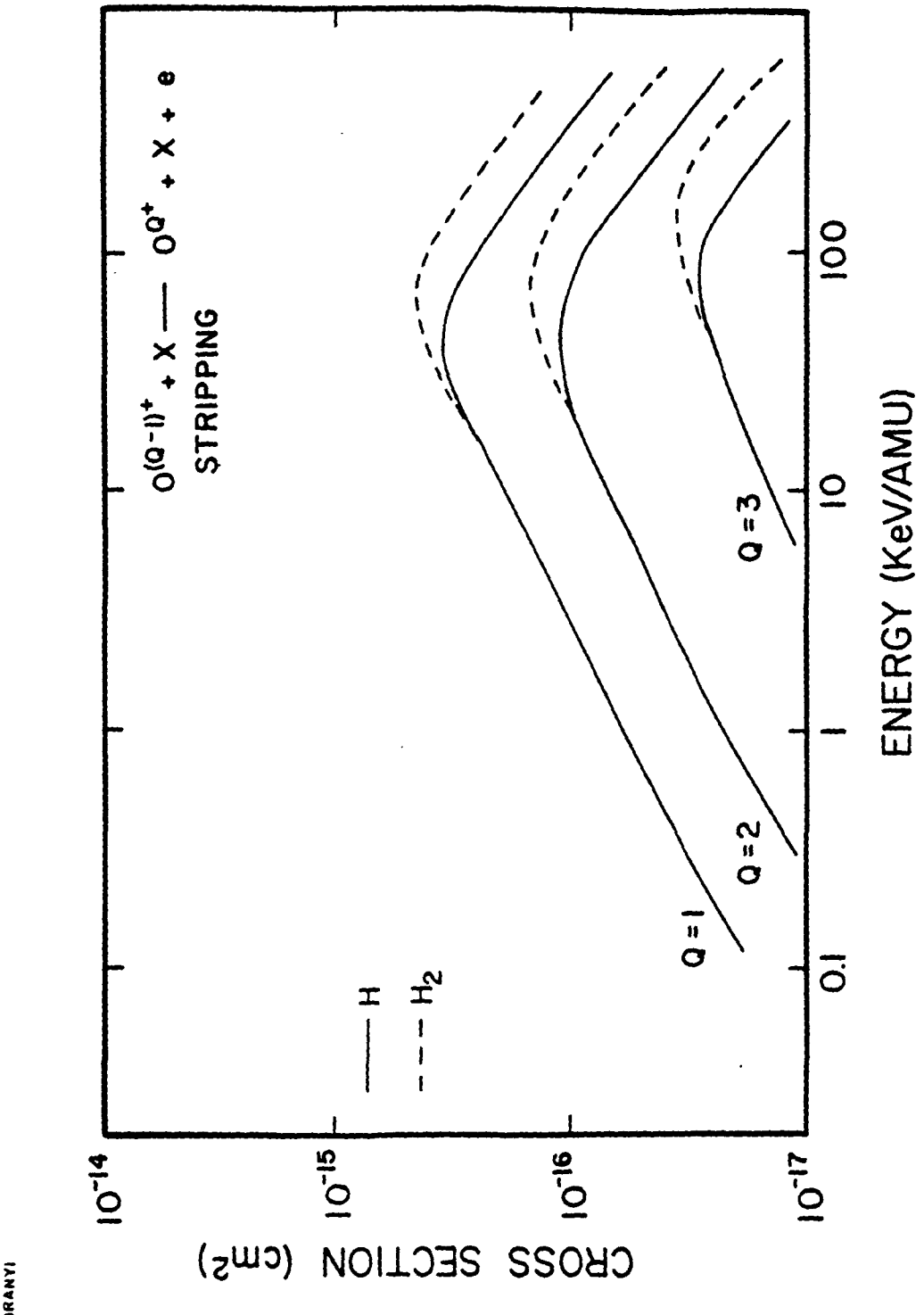
$O^{(Q-1)+} + X \longrightarrow O^{Q+} + X + e$
STRIPPING
H
H_2
Q=1
Q=2
Q=3
CROSS SECTION (cm^2)
10^{-14}
10^{-15}
10^{-16}
10^{-17}
0.1
1
10
100
ENERGY (KeV/AMU)
HORANYI

FIGURE 4

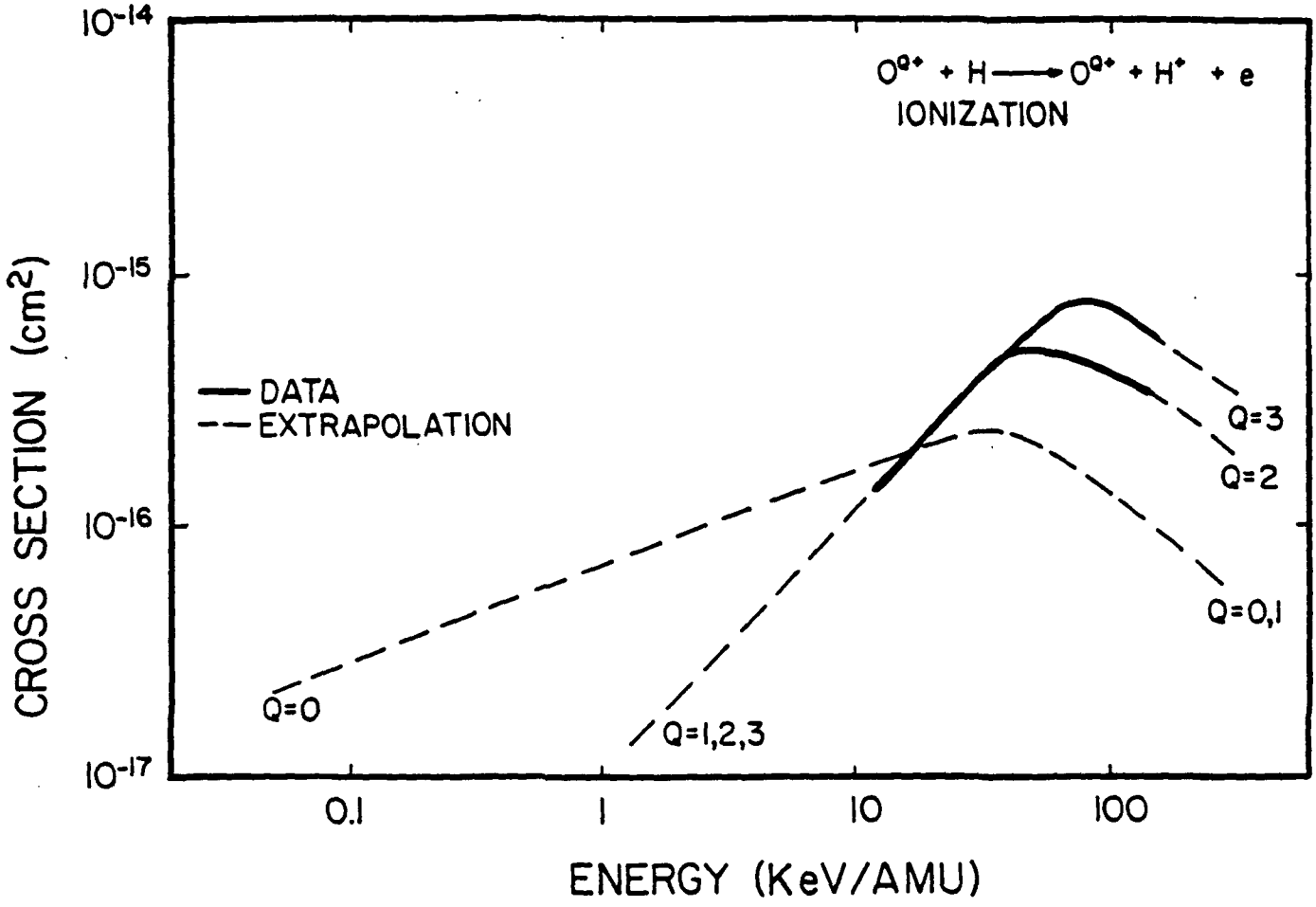
$O^{q+} + H \longrightarrow O^{q+} + H^+ + e$
IONIZATION
CROSS SECTION (cm^2)
10^{-14}
10^{-15}
10^{-16}
10^{-17}
DATA
EXTRAPOLATION
Q=3
Q=2
Q=0,1
Q=0
Q=1,2,3
0.1
1
10
100
ENERGY (KeV/AMU)

FIGURE 5

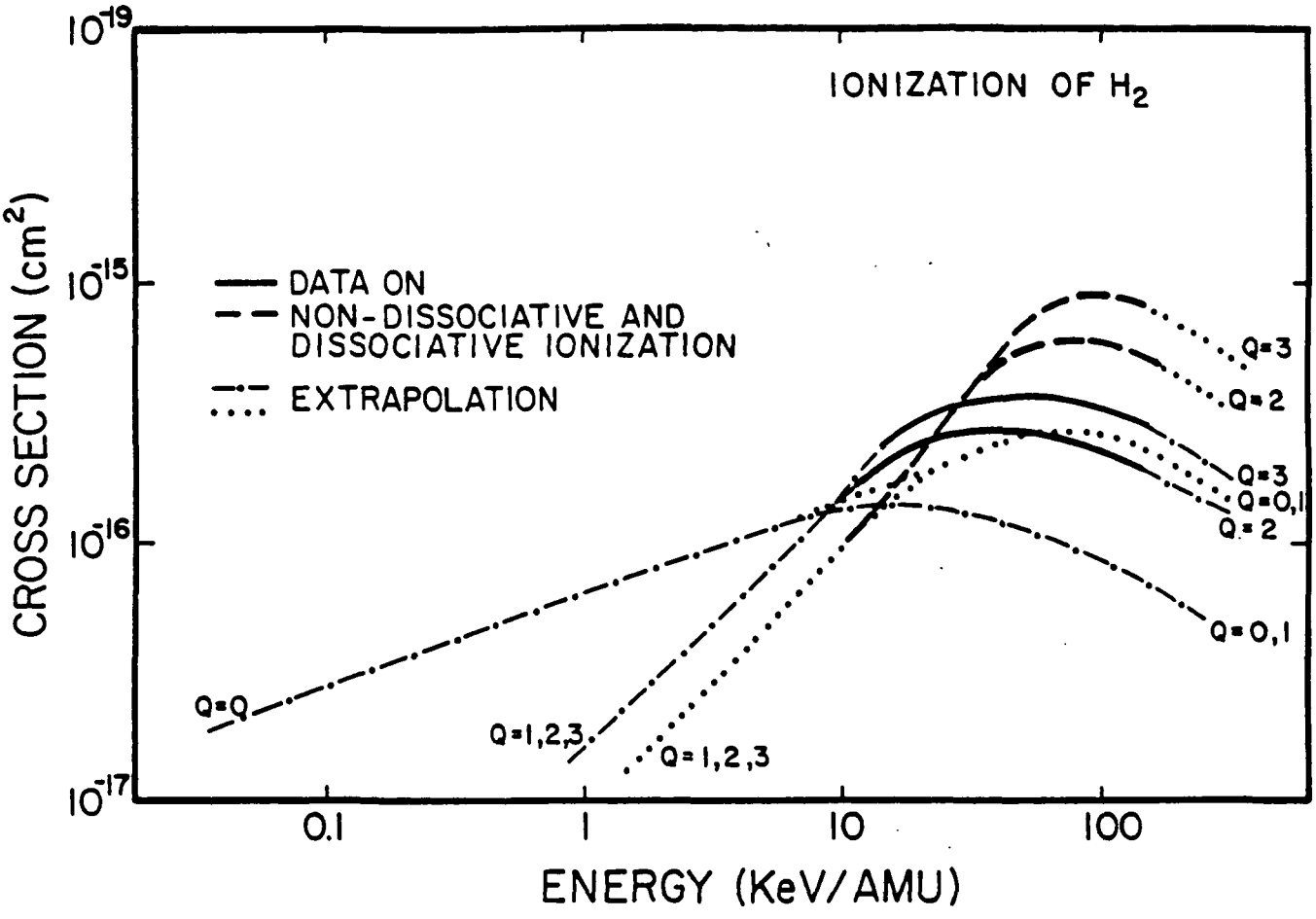
IONIZATION OF H_2
DATA ON
NON-DISSOCIATIVE AND DISSOCIATIVE IONIZATION
EXTRAPOLATION
CROSS SECTION (cm^2)
10^{-15}
10^{-16}
10^{-17}
0.1
1
10
100
ENERGY (KeV/AMU)
Q=3
Q=2
Q=3
Q=0,1
Q=2
Q=0,1
Q=0
Q=1,2,3
Q=1,2,3

FIGURE 6

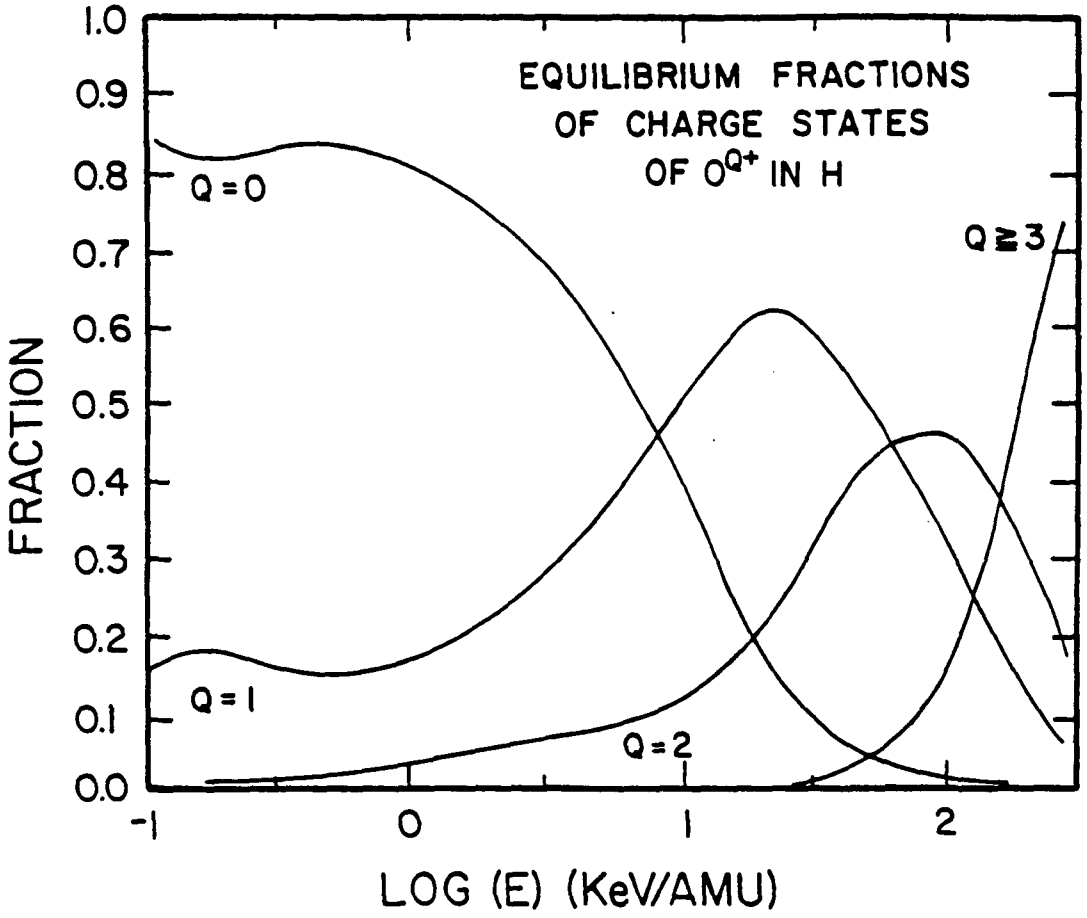
EQUILIBRIUM FRACTIONS
OF CHARGE STATES
OF O^{Q+} IN H
Q = 0
Q = 1
Q = 2
Q ≥ 3
FRACTION
LOG (E) (KeV/AMU)
1.0
0.9
0.8
0.7
0.6
0.5
0.4
0.3
0.2
0.1
0.0
-1
0
1
2

FIGURE 7

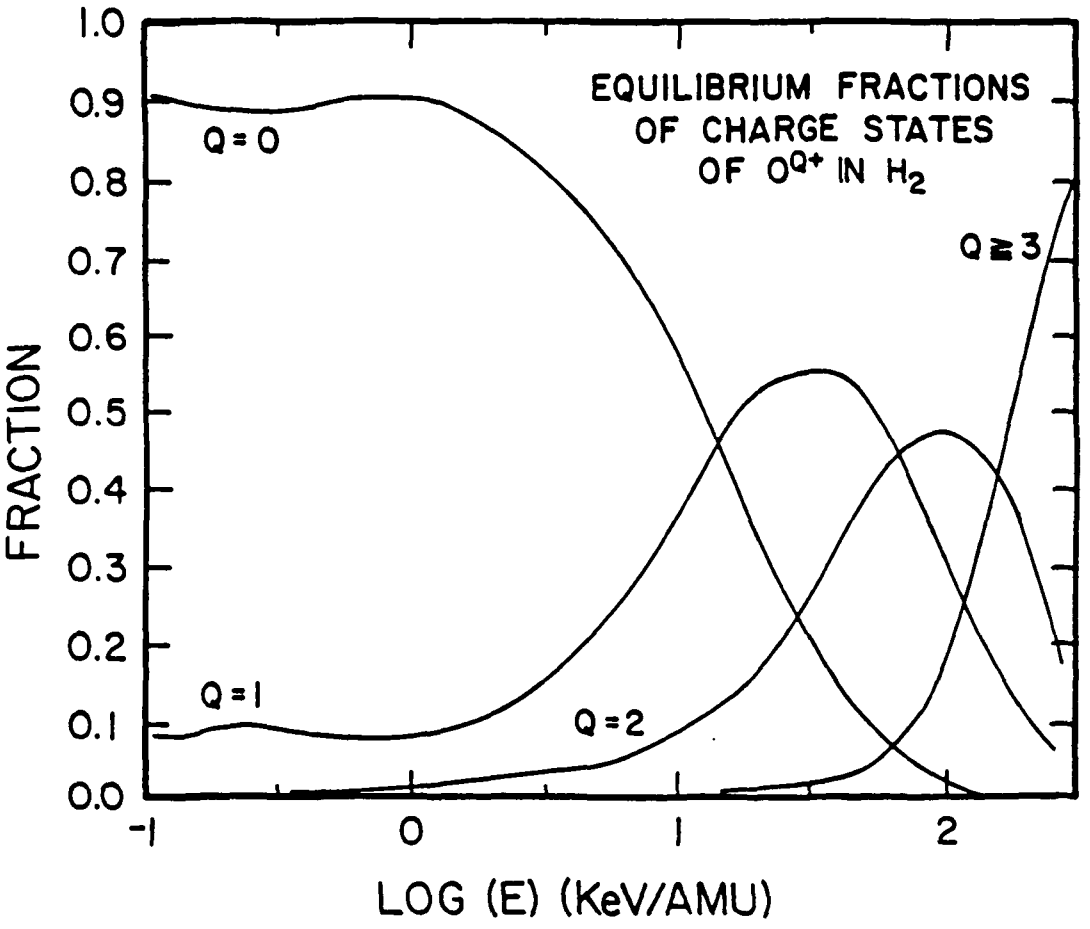
EQUILIBRIUM FRACTIONS
OF CHARGE STATES
OF O^{Q+} IN H_2
Q = 0
Q = 1
Q = 2
Q ≥ 3
FRACTION
LOG (E) (KeV/AMU)
1.0
0.9
0.8
0.7
0.6
0.5
0.4
0.3
0.2
0.1
0.0
-1
0
1
2

FIGURE 8

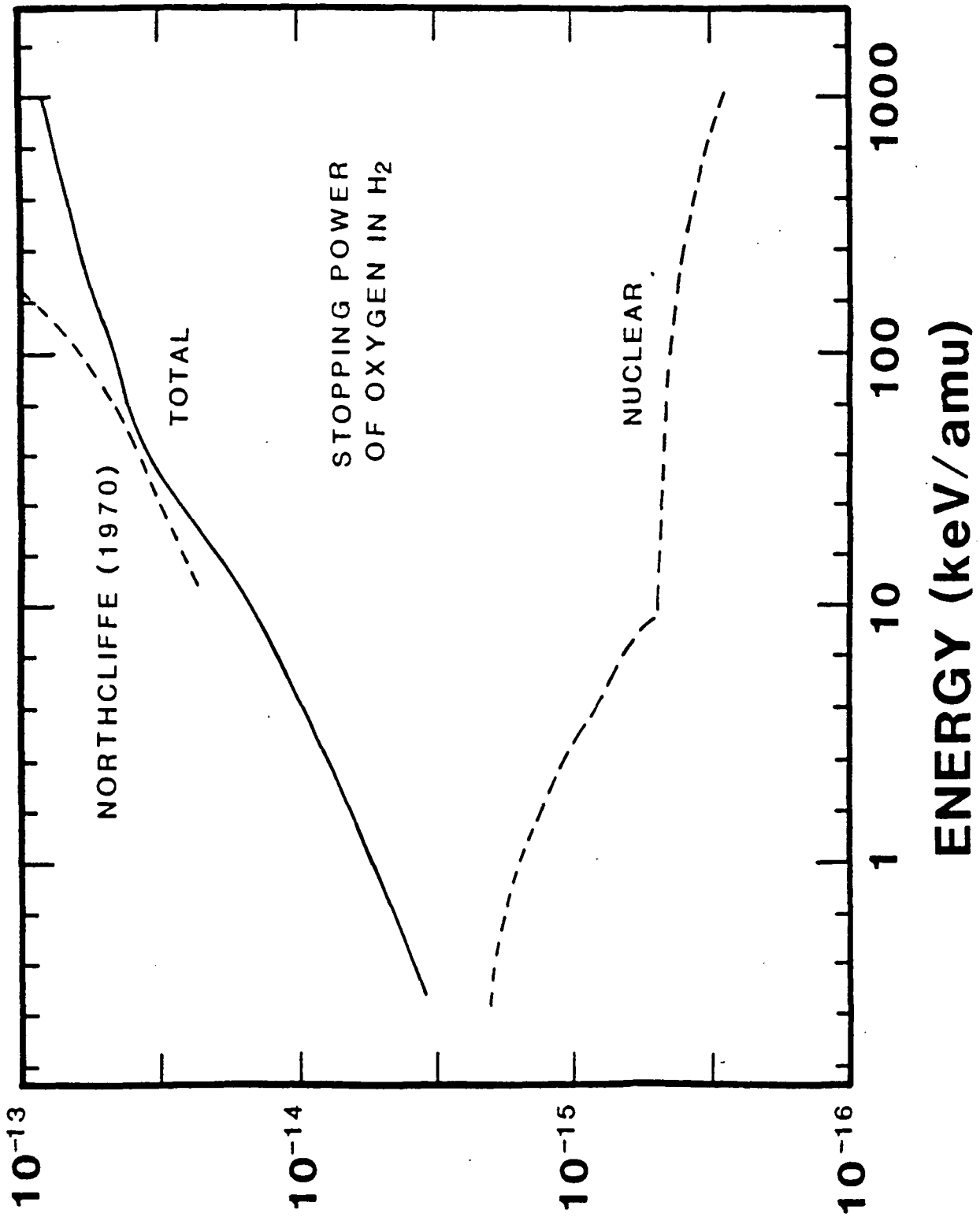

FIGURE 9

CRAVENS

CRAVENS

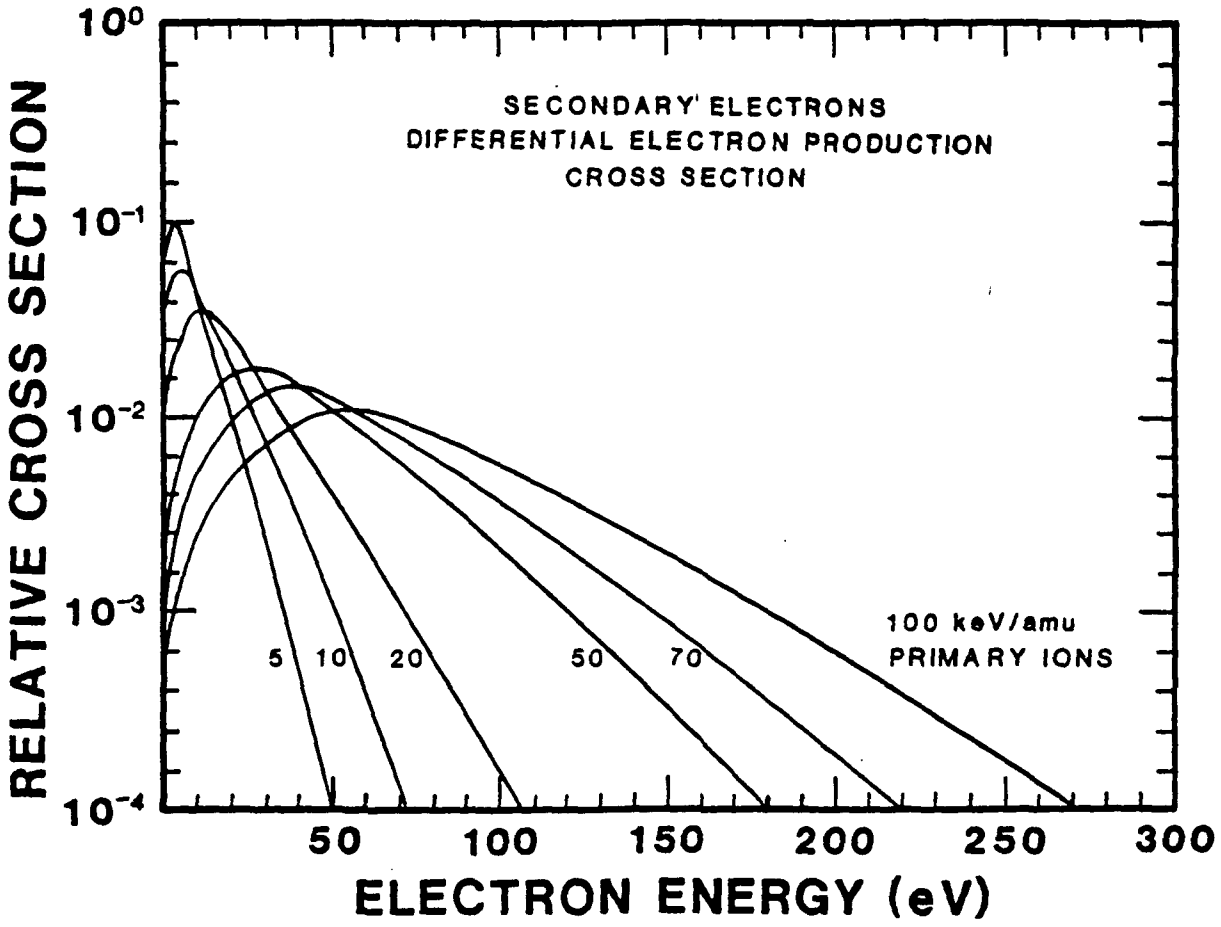

FIGURE 10

CRAVENS

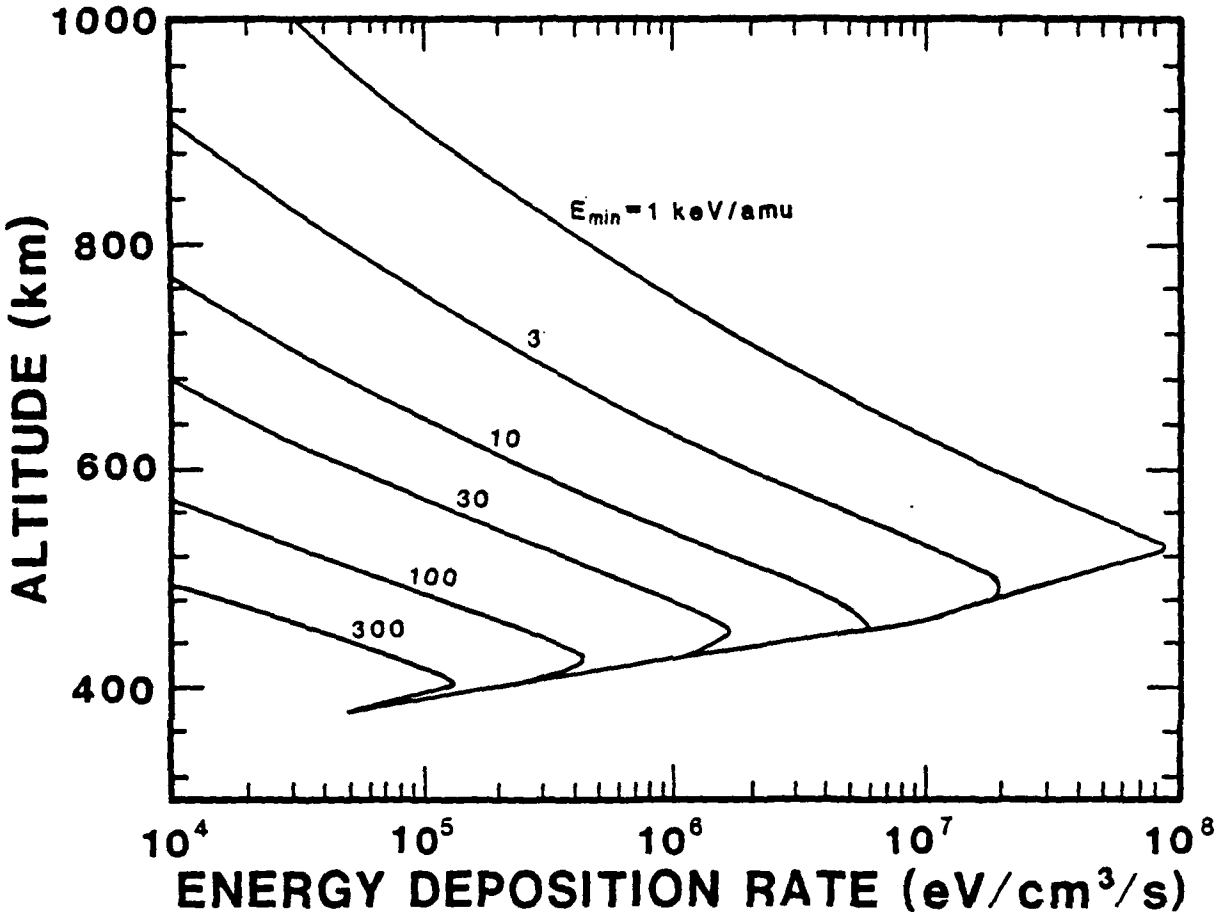

FIGURE 11

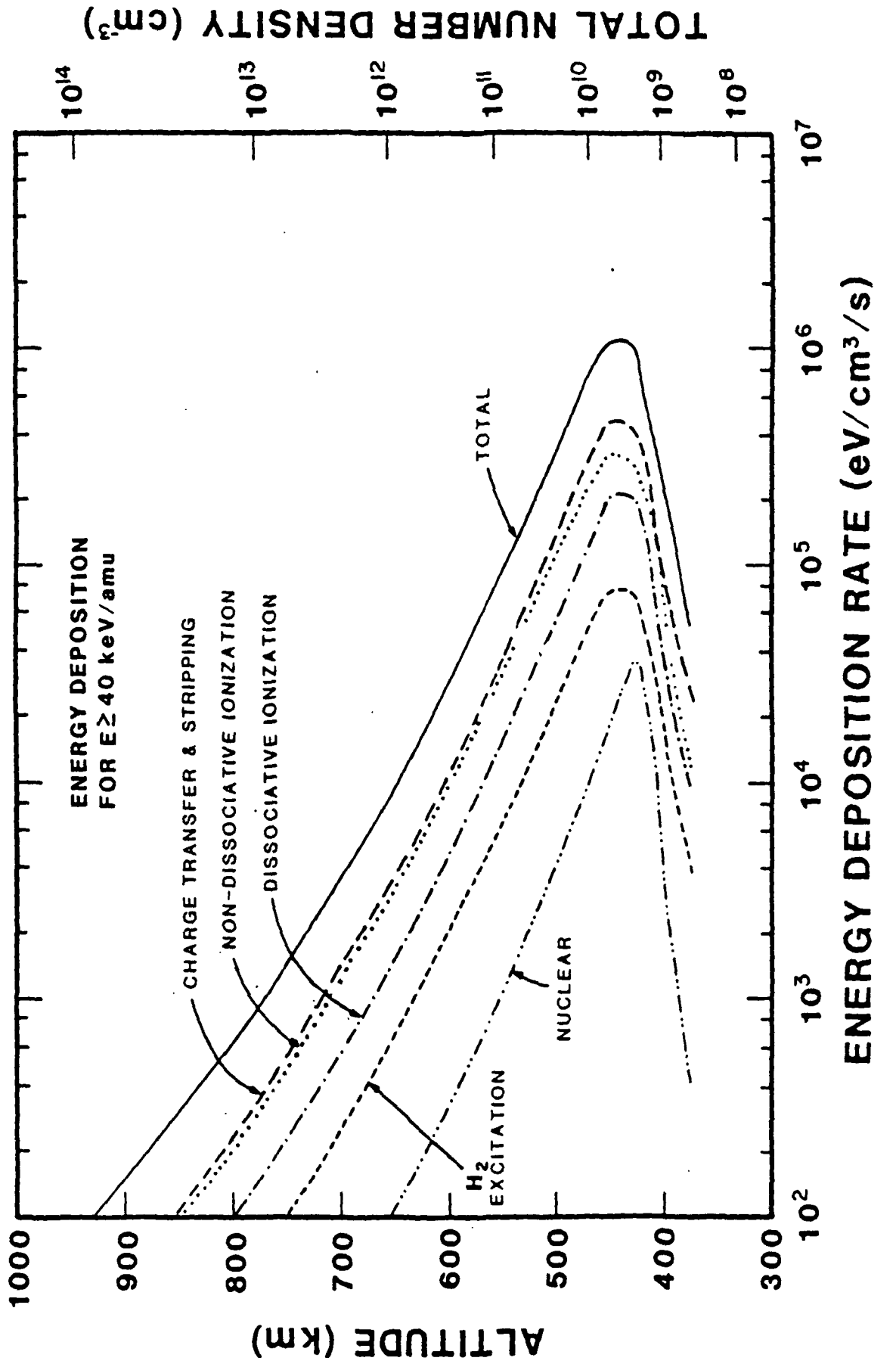
TOTAL NUMBER DENSITY (cm⁻³)
10¹⁴
10¹³
10¹²
10¹¹
10¹⁰
10⁹
10⁸
10⁷
ENERGY DEPOSITION RATE (eV/cm³/s)
10⁶
10⁵
10⁴
10³
10²
ALTITUDE (km)
1000
900
800
700
600
500
400
300
ENERGY DEPOSITION
FOR E≥ 40 keV/amu
TOTAL
CHARGE TRANSFER & STRIPPING
NON-DISSOCIATIVE IONIZATION
DISSOCIATIVE IONIZATION
NUCLEAR
H2 EXCITATION

FIGURE 12

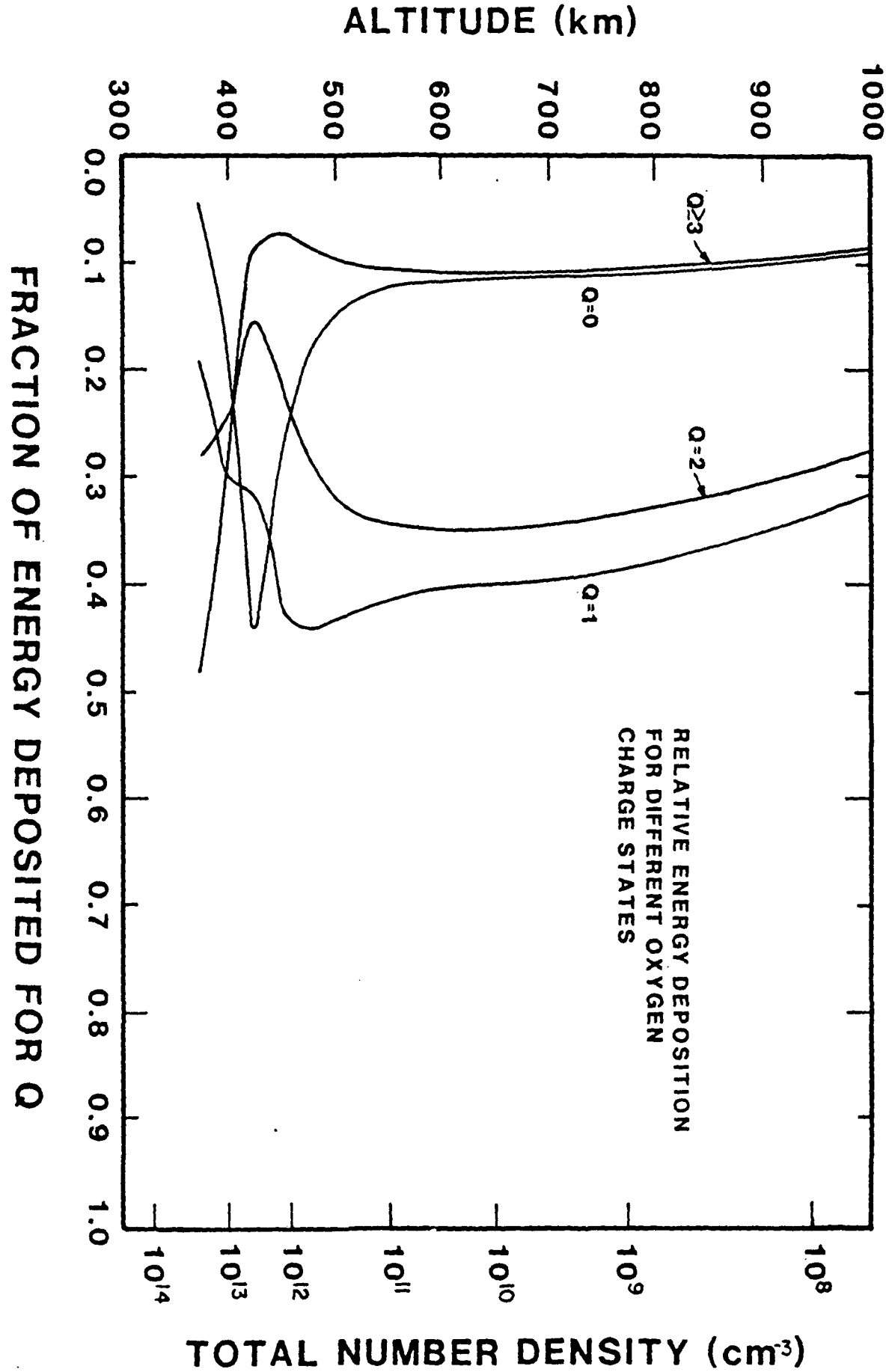
ALTITUDE (km)
300
400
500
600
700
800
900
1000
FRACTION OF ENERGY DEPOSITED FOR Q
0.0
0.1
0.2
0.3
0.4
0.5
0.6
0.7
0.8
0.9
1.0
Q≥3
Q=0
Q=2
Q=1
RELATIVE ENERGY DEPOSITION
FOR DIFFERENT OXYGEN
CHARGE STATES
10^{14}
10^{13}
10^{12}
10^{11}
10^{10}
10^{9}
10^{8}
TOTAL NUMBER DENSITY (cm^{-3})

FIGURE 13

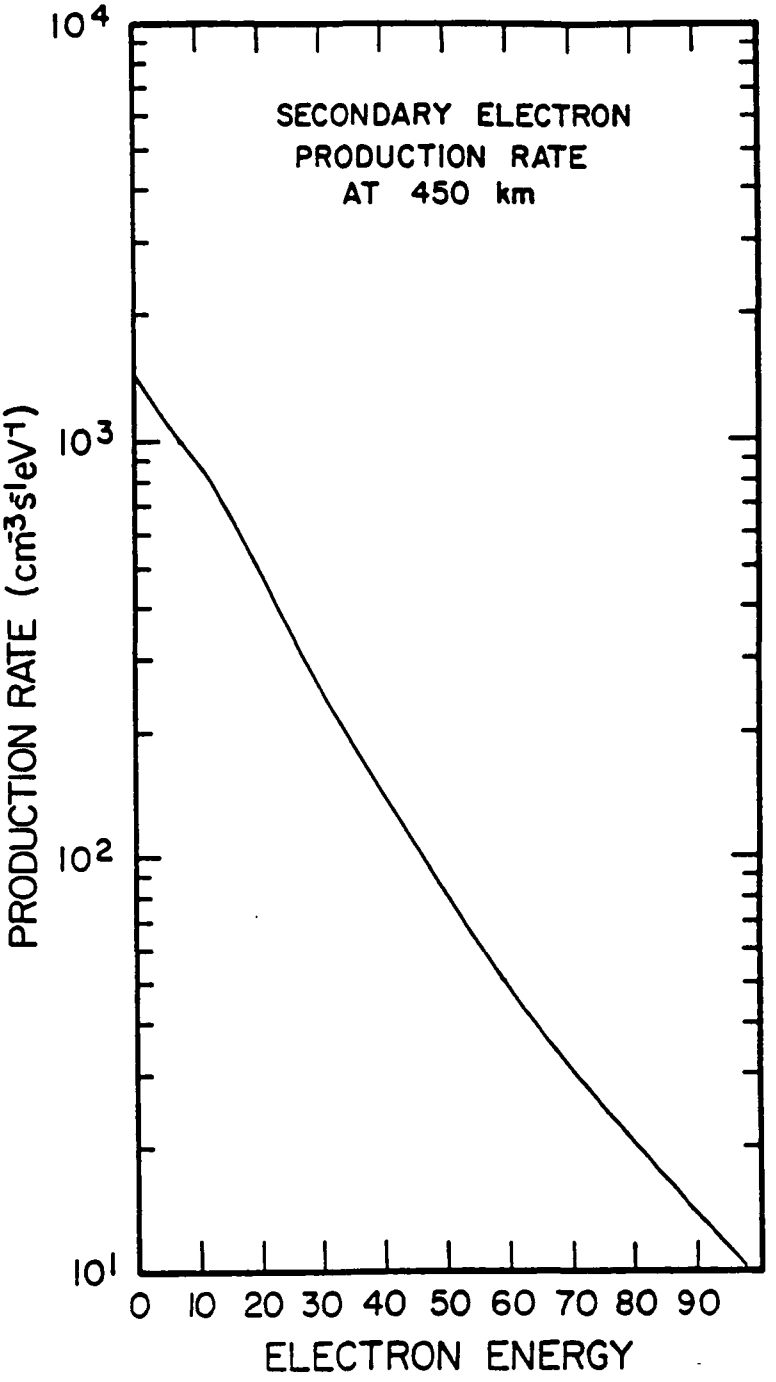
SECONDARY ELECTRON
PRODUCTION RATE
AT 450 km
PRODUCTION RATE (cm^{-3}s^{-1}eV^{-1})
10^4
10^3
10^2
10^1
0 10 20 30 40 50 60 70 80 90
ELECTRON ENERGY

FIGURE 14

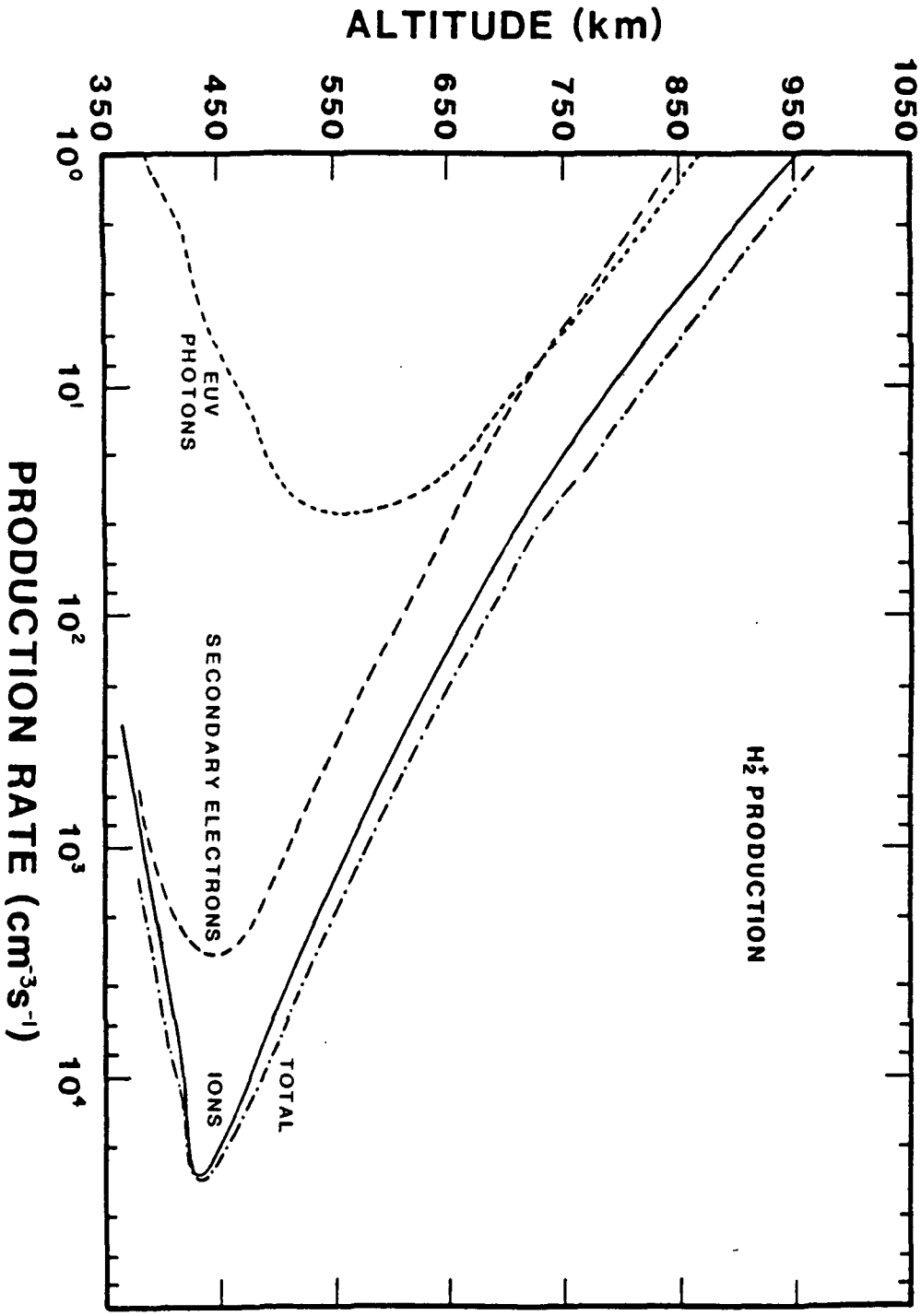
ALTITUDE (km)
350
450
550
650
750
850
950
1050
PRODUCTION RATE (cm⁻³s⁻¹)
10⁰
10¹
10²
10³
10⁴
EUV PHOTONS
SECONDARY ELECTRONS
IONS
TOTAL
H₂⁺ PRODUCTION

FIGURE 15

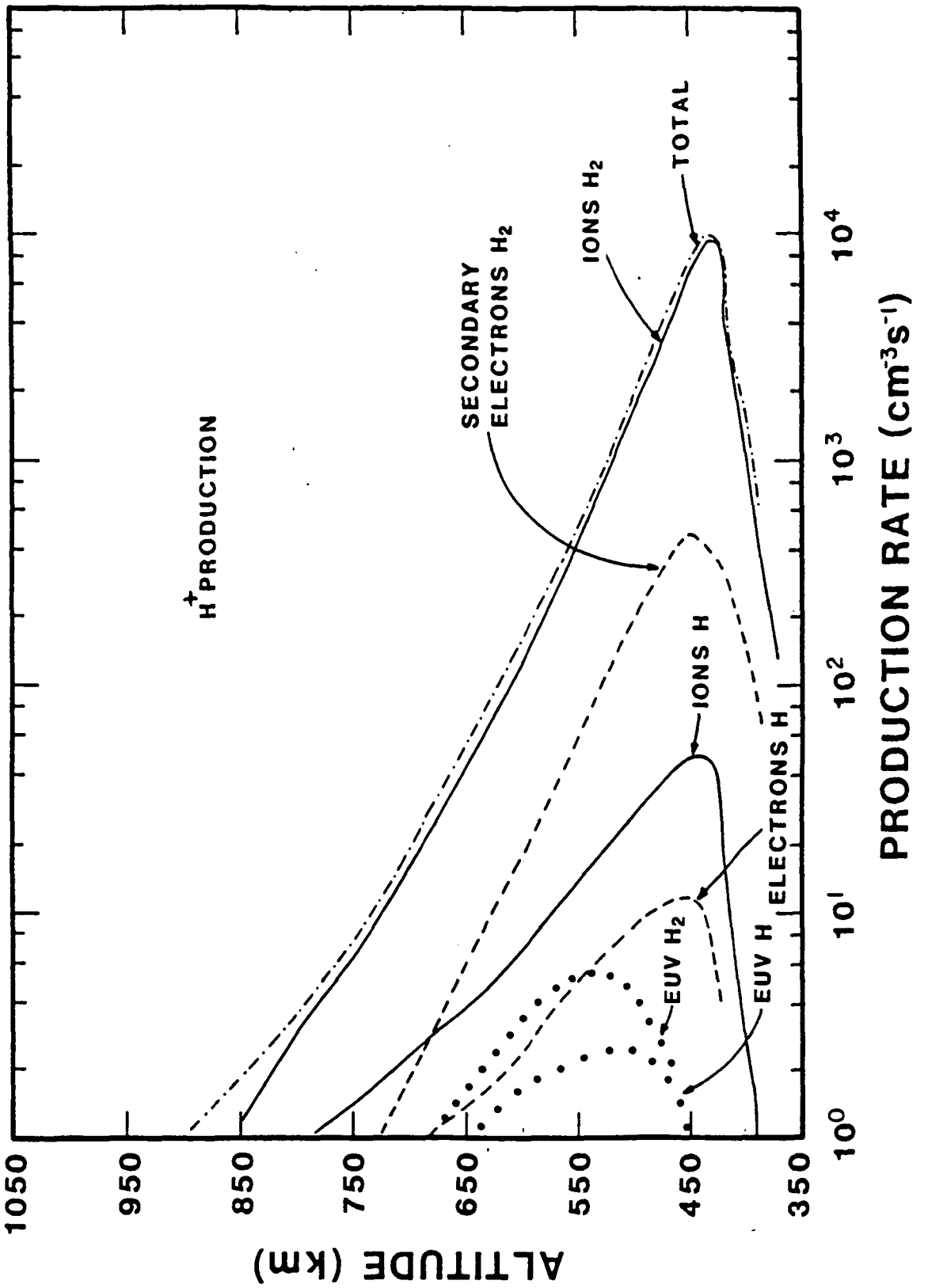
ALTITUDE (km)
1050
950
850
750
650
550
450
350
PRODUCTION RATE ($cm^{-3}s^{-1}$)
10^0
10^1
10^2
10^3
10^4
H^+ PRODUCTION
SECONDARY ELECTRONS H_2
IONS H_2
TOTAL
IONS H
ELECTRONS H
EUV H_2
EUV H

FIGURE 16

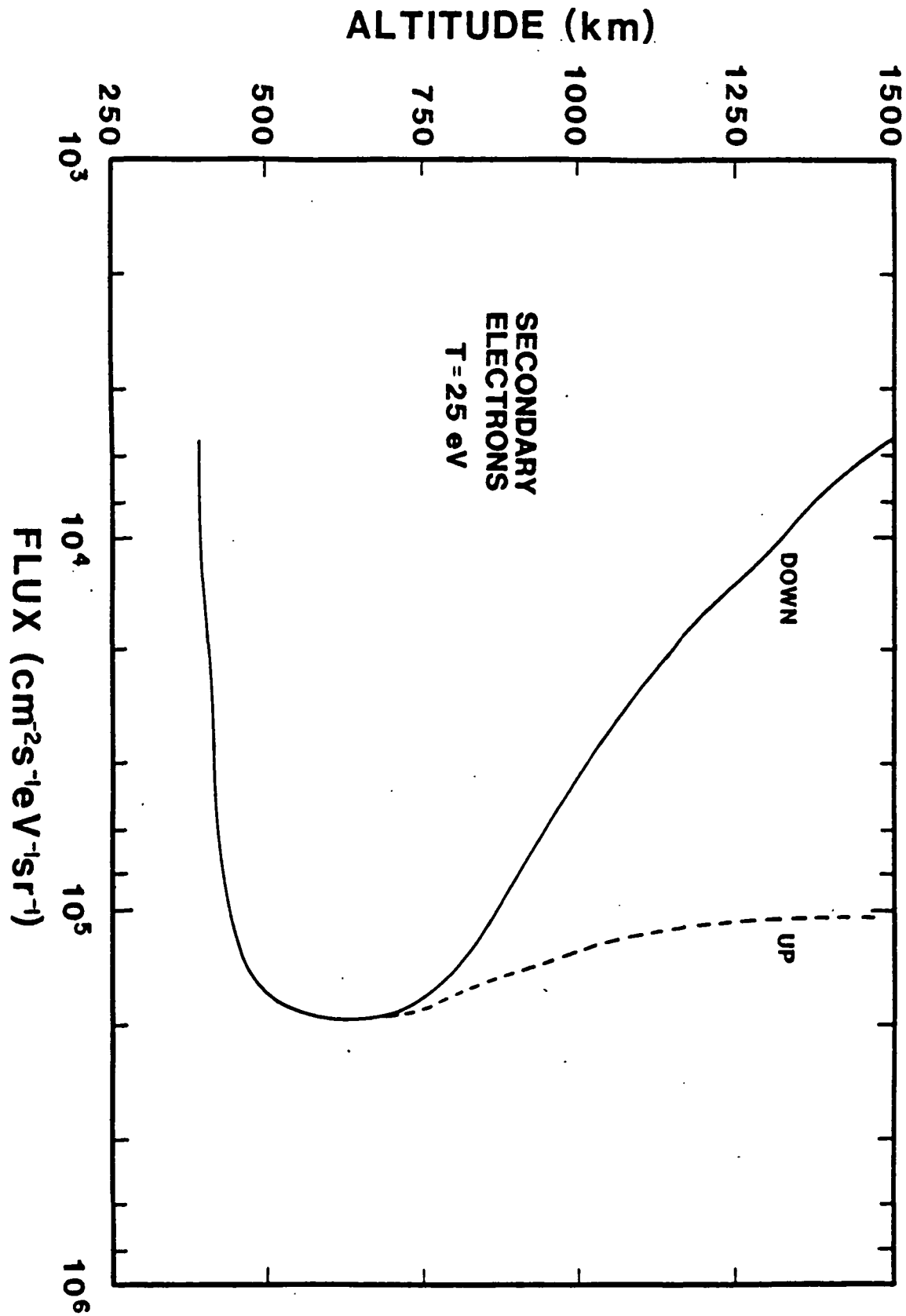
ALTITUDE (km)
250
500
750
1000
1250
1500
10^3
10^4
10^5
10^6
FLUX ($cm^{-2}s^{-1}eV^{-1}sr^{-1}$)
SECONDARY ELECTRONS
T=25 eV
DOWN
UP

FIGURE 17

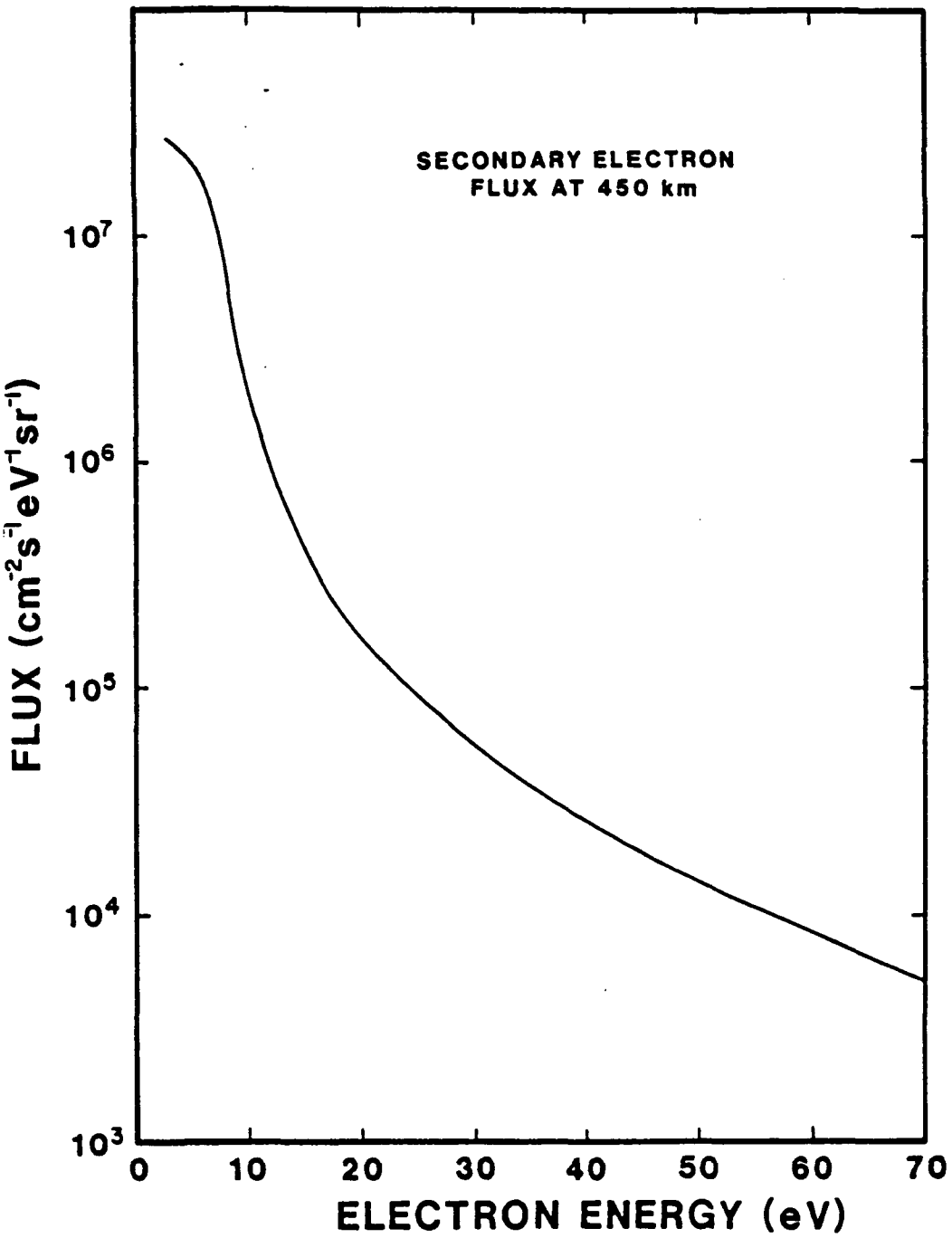
SECONDARY ELECTRON
FLUX AT 450 km
FLUX (cm^{-2}s^{-1}eV^{-1}sr^{-1})
10^7
10^6
10^5
10^4
10^3
0
10
20
30
40
50
60
70
ELECTRON ENERGY (eV)

FIGURE 18

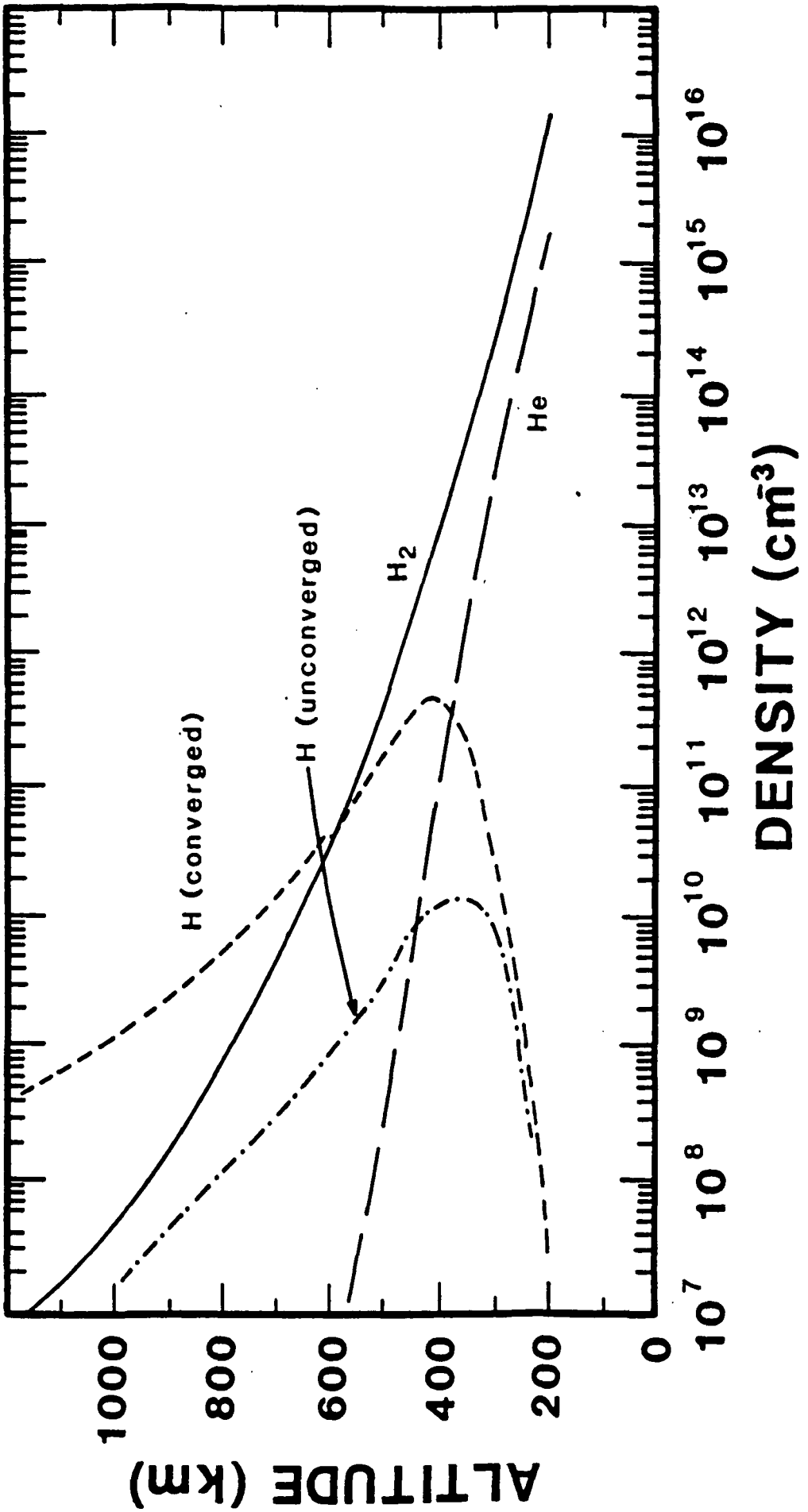
ALTITUDE (km)
0
200
400
600
800
1000
DENSITY (cm⁻³)
10⁷
10⁸
10⁹
10¹⁰
10¹¹
10¹²
10¹³
10¹⁴
10¹⁵
10¹⁶
H (converged)
H (unconverged)
H₂
He

FIGURE 19

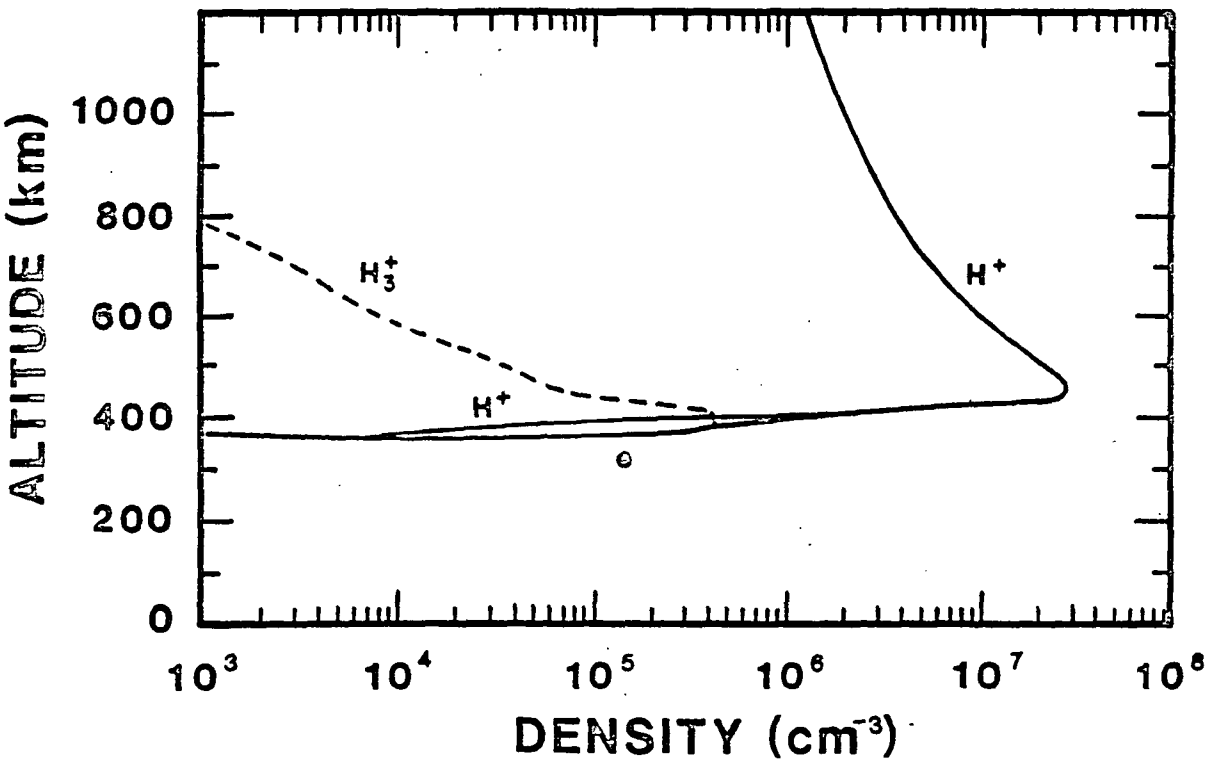
ALTITUDE (km)
1000
800
600
400
200
0
H_3^+
H^+
H^+
O
10^3
10^4
10^5
10^6
10^7
10^8
DENSITY (cm^{-3})

FIGURE 20

TABLE 1

Initial Beam Energies

k	E_k(keV/amu)		
1	0.3	25	230.0
2	1.0	26	260.0
3	2.0	27	300.0
4	3.0	28	340.0
5	4.0	29	360.0
6	5.0	30	400.0
7	6.0	31	440.0
8	7.0	32	460.0
9	8.0	33	500.0
10	9.0	34	530.0
11	10.0	35	560.0
12	15.0	36	600.0
13	20.0	37	630.0
14	30.0	38	660.0
15	40.0	39	700.0
16	50.0	40	730.0
17	60.0	41	760.0
18	70.0	42	800.0
19	80.0	43	830.0
20	90.0	44	860.0
21	100.0	45	900.0
22	130.0	46	930.0
23	160.0	47	960.0
24	200.0	48	1000.0

TABLE 2a

Column Energy Deposition for Unconverged Atmosphere

Process	Column Production Rate($cm^{-2}s^{-1}$) Primaries	Secondaries	Total	Energy Efficiency
Energy Input	9.25x10^{12} eV	3.27x10^{12} eV(35%)	9.25(12)eV	100.0%
Backscattered Electrons	--	5.58(8)eV*	5.58(8)eV	≈ 0.0%
Lyman Bands	2.05(10)**	1.83(10)	3.88(10) (65.7kR)	4.0%
Werner Bands	1.51(10)	1.18(10)	2.69(10)	3.0%
Lyman alpha	8.97(9)	5.64(9)	1.46(10)	1.6%
H_2^+	1.61(11)	3.09(10)	1.92(11)	33.0%
$H^+(H_2)$	5.17(10)	4.37(9)	5.61(10)	12.4%
$H^+(H)$	5.49(8)	1.54(8)	7.03(8)	0.1%
Vibrational*** Excit. (direct)	--	1.57(12)	1.57(12)	9.2%
Vibrational*** Excit. (cascade)	1.59(11)	1.35(11)	2.94(11)	1.7%
$H(H_2$,direct)	5.17(10)	1.70(11)	2.24(11)	5.1%
Electron Heat	--	2.00(11)eV	2.00(11)eV	2.2%
Neutral Heat (direct)	3.36(11)eV	6.12(11)eV	9.48(11)eV	10.3%
OI,II,III Excit.	9.30(11)eV	--	9.30(11)eV	10.0%
Nuclear/Elastic				

(neutral heat)	1.76(11)eV	--	1.76(11)eV	1.9%
Misc.	--	--	--	5.5%
				100.0%

* 5.58(8)eV should be read as 5.58×10^8 eV/cm^2/s

** 2.05(10) should be read as 2.05×10^{10} cm^{-2}s^{-1}

*** Total number of vibrational quanta produced

TABLE 2b

Column Energy Deposition for Converged Atmosphere

Process	Column Production Rate ($cm^{-2}s^{-1}$) Primaries	Secondaries	Total	Energy Efficiency
Energy Input	9.25×10^{12} eV	3.05×10^{12}eV(33%)	9.25(12)eV	100.0%
Backscattered Electrons	--	2.08(8) eV*	2.08(8) eV	≈ 0%
Lyman Bands	1.73(10)**	1.43(10)	3.16(10) (53.7kR)	3.3%
Werner Bands	1.27(10)	9.43(9)	2.21(10)	2.5%
Lyman alpha	2.50(10)	9.21(9)	3.42(10) (38.4kR)	3.8%
H_2^+	1.36(11)	2.44(10)	1.60(11)	27.7%
$H^+(H_2)$	4.39(10)	3.49(9)	4.74(10)	10.5%
$H^+(H)$	2.95(10)	7.05(9)	3.66(10)	8.1%
Vibrational*** Excit. (direct)	--	7.93(11)	7.93(11)	4.6%
Vibrational*** Excit. (cascade)	1.56(11)	1.02(11)	2.58(11)	1.5%
$H(H_2$, direct)	4.39(10)	1.29(11)	1.74(11)	4.3%
Electron Heat	--	5.28(11)eV	5.28(11)eV	5.7%
Neutral Heat (direct)	2.85(11)eV	4.70(11)eV	7.55(11)eV	8.2%

OI,II,III Excit.	9.30(11)eV	--	9.30(11)eV	10.0%
Nuclear/Elastic (neutral heat)	1.70(11)eV	--	1.70(11)eV	1.8%
Misc.	--	--	--	8.0%
				100.0%

* 2.08(8)eV should be read as 2.08×10^{8} eV/cm^2/s

** 1.73(10) should be read as 1.73×10^{10} cm^{-2}s^{-1}

*** Total number of vibrational quanta produced

TABLE 3

Comparison of Energy Efficiencies for Ion and Electron Precipitation into the Unconverged Atmosphere for Selected Processes

Process	Oxygen (E≥40 keV/amu)	10 keV electrons
H_2^+	33.0%	38.9%
H+(total)	12.5%	2.8%
Lyman/Werner bands	7.0%	14.5%
OI,II,III excitation	10.0%	0.0%
(all vibration + direct neutral heat + electron heat)	23.4%	24.4%
direct H production	5.1%	6.1%